

Excitons in a disordered medium: A numerical study in InGaN quantum wells

Aurelien David ^{1,*} and Claude Weisbuch ^{2,3}

¹Google, 1600 Amphitheater Pkwy, Mountain View, California 94043, USA

²Materials Department, University of California, Santa Barbara, California 93106, USA

³Laboratoire de Physique de la Matière Condensée, CNRS, IP Paris, Ecole Polytechnique, 91128 Palaiseau, France



(Received 13 May 2022; revised 31 August 2022; accepted 1 September 2022; published 4 October 2022)

Excitons in InGaN quantum wells are investigated numerically, considering random alloy disorder and Coulomb interaction on equal footing in the Schrödinger equation. Their statistical properties are systematically explored as a function of the quantum well thickness and composition, revealing a complex competition between disorder-induced carrier localization, Coulomb attraction, and field-induced wave function separation. This results in a class of semiconductor quasiparticle with hybrid properties in between hydrogenoid excitons and disorder-localized free particles. Exciton screening by free carriers is investigated and shows distinct behavior from the screening of bulk excitons. Finally, a highly accurate approximate solution of the excitonic Schrödinger equation, with reduced numerical complexity, is introduced.

DOI: [10.1103/PhysRevResearch.4.043004](https://doi.org/10.1103/PhysRevResearch.4.043004)

I. INTRODUCTION

Excitons have garnered considerable interest in semiconductor physics. They are the elementary excitations of electron-hole pairs across the bandgap, considering the Coulomb interaction. [1]. This leads to hydrogenoid relative motion of the electron and hole and to a Rydberg series of energy levels. In conventional III–V semiconductors, they dominate the optical properties at low temperature [2].

Modern semiconductor devices complicate the simple excitonic picture. First, many applications make use of heterostructures with ultrathin layers such as quantum wells (QWs), where quantum confinement occurs alongside the Coulomb interaction; the competition between both phenomena can be gauged by comparing the excitonic Bohr radius to the QW thickness. Additionally, due to epitaxial constraints, ternary semiconductor alloys are commonly used to make these heterostructures. These feature inherent disorder—the so-called *random alloy disorder*, whose effects further influence the Coulomb interaction.

Treatment of the interplay between disorder and the Coulomb interaction is easiest when one effect dominates the other. In the limiting case of very strong disorder, electrons and holes are localized, and the Coulomb interaction barely affects the wave functions. The opposite limiting case of weak disorder is conventionally analyzed using the virtual crystal approximation, i.e., a perfectly ordered crystal whose properties average those of binary compounds. This approximation

ignores spatial compositional fluctuations and the disordered potentials and carrier localization they induce. The impact of alloy effects on excitonic properties can then be treated perturbatively since the random potential is small compared with the exciton binding energy [3,4]. In addition to III–Vs, the interplay between excitons and disorder has attracted interest in other material systems. This includes II–VI semiconductors [5] and two-dimensional (2D) inorganic semiconductors [6] as well as organic materials such as J-aggregates [7,8] and polymers [9]. In many such studies, the excitonic interaction dominates, and the exciton is treated as the elementary particle in theoretical models; the internal structure of the excitonic wave function is often not considered.

Of particular interest is the intermediate regime where localization and Coulomb attraction are of the same order. There, one can expect excitons to possess complex behavior, borrowing both from the physics of hydrogenoid excitons and of localized carriers. However, this regime has barely been investigated, perhaps in part owing to its complexity.

Wide-bandgap III-nitride semiconductors are an ideal testbed to explore this regime. First, they feature a large binding energy (20 meV in bulk GaN) [10]. This makes excitons potentially stable at room temperature, opening the question of their influence on classical light emitters [i.e., light emitting diodes (LEDs)] and their possible use in quantum devices [11–18]. Second, and crucially, the random alloy disorder in III-nitride heterostructures with ternary compounds (e.g., InGaN, AlGaIn, AlInN) results in energy fluctuations of tens of millielectronvolts (meV) across a few nanometers, which decorrelate the electron-hole relative motion. This leads to partial and separate localization of the electron and hole, further affecting their interaction. This fulfills the intermediate regime where disorder and Coulomb energies are of the same order of magnitude. In addition, the polarization fields induced by heterostructures lead to a separation of electrons and holes, which decreases the Coulomb interaction. This

*aureliendavid@google.com

Published by the American Physical Society under the terms of the [Creative Commons Attribution 4.0 International](https://creativecommons.org/licenses/by/4.0/) license. Further distribution of this work must maintain attribution to the author(s) and the published article's title, journal citation, and DOI.

results in a complex material system, where the respective effects of Coulomb interaction, disorder-induced localization, and polarization fields all compete in determining the nature of the semiconductor quasiparticles.

In practice, these considerations lead to an excitonic Schrödinger equation that cannot be solved perturbatively, i.e., a computational problem in six dimensions (6D) without symmetry reductions (precluding the separation of the relative and absolute motions [1]), which is very challenging from a computational standpoint.

The physics resulting from polarization fields and alloy disorder in III-nitride QWs have been studied theoretically in the past decade. However, the vast majority of these investigations consider free electrons and holes, ignoring the Coulomb interaction, a much-simpler three-dimensional (3D) problem [19–24]. In general, it is concluded that holes are tightly localized by disorder, whereas electrons are nearly free (i.e., with a large lateral extent in the QW plane). A few studies have explored the effect of the Coulomb interaction in InGaN quantum dots and wells [18,25–27] with a model that seeks to reconstructs the excitonic wave function using a basis of free-particle states (an approach, however, whose accuracy has not been fully established). Recently, one of the present authors presented a method to solve the 6D problem directly and showed that considering the Coulomb interaction was essential to explain the radiative properties of InGaN LEDs [28].

Nonetheless, a quantitative understanding of the nature of excitons in III-nitride QWs remains lacking. Many works assume an exciton binding energy of several tens of meV (motivated by models that ignore alloy disorder [29,30]), but it is unclear how this value and the related properties of the excitonic wave functions are affected by the QW design and how much they vary statistically due to disorder.

In this paper, we perform a numerical study of excitons in InGaN QWs. We first introduce a numerical method to solve the 6D Schrödinger equation in the presence of disorder. We then compute a large number of excitonic wave functions to study excitonic properties in a variety of configurations, revealing a complex dependence on the QW design (i.e., its composition and thickness). We explore the effect of screening by free carriers, which reduces excitonic effects at high density. Finally, we discuss an efficient simplification of the computational problem through dimensionality reduction [31].

II. NUMERICAL METHOD

A. Outline

Our general approach is to solve the Schrödinger equation in the two-band envelope function approximation, with a finite-difference discretization in real space, considering alloy fluctuation and the Coulomb interaction.

We consider InGaN single-QW samples, of varying thickness and composition, embedded in a GaN *pin* junction with an intrinsic thickness of 20 nm and an applied forward bias of 3 V. These conditions are reasonably representative of a single-QW LED structure under electrical or optical injection.

The growth direction is along z , with the QW plane in the lateral directions (x, y) .

We use a Cartesian finite-difference computation domain, with dimensions $L_x = L_y = 18$ nm, $L_z = 10$ nm, and mesh steps $dx = dy = 0.6$ nm, $dz = 0.3$ nm. These mesh values are sufficient to retain good numerical accuracy; the domain size is sufficient to compute wave functions with minimal effects from the boundaries of the domain.

The potential seen by the electrons and holes has several contributions: the potential energy V_0 due to the semiconductor band structure, the potentials V_J and V_P corresponding to the junction field and polarization fields, and the Coulomb interaction potential V_C .

Here, V_0 is generated with a method described in previous works [19,22]: given a QW with a nominal thickness and composition, we first generate a random distribution of In and Ga atoms on a fine 3D square grid with a spacing of 0.3 nm. This atomic composition map is then averaged by a Gaussian function with $\sigma = 0.3$ nm (this specific value is not critical for the results, as discussed in Appendix A) to yield the smooth potential seen by the envelope functions. We call such a map a *configuration* (each configuration corresponds to a different random generation of atoms). Note that the In composition varies along the growth direction inside the QW. Figure 1(a) shows an in-plane cross-section (at a given z) of such a smoothed composition map. This map is then down-sampled to the coarser finite-difference grid described above. Due to the statistical distribution, the QW does not have sharp heterointerfaces along the growth direction but instead transitions smoothly from InGaN to GaN over a scale of ~ 1 nm [Fig. 1(b)]. Accordingly, the QW width is defined as the full width at half maximum of the In composition after averaging in-plane.

The electrostatic potentials V_J and V_P are computed by a conventional approach, detailed in Appendix A.

The Coulomb potential is, in principle, given by the conventional expression $V_C = -e^2/4\pi\epsilon_0\epsilon_r$, with $r = |\mathbf{r}_h - \mathbf{r}_e|$ the electron-hole separation. However, a naive discretization of V_C fails numerically since it diverges at points where $\mathbf{r}_e = \mathbf{r}_h$. This is a well-known difficulty in treating the Coulomb potential, and several regularization schemes have been explored over the decades to circumvent it [32,33]. We have found that the so-called ABC scheme proposed in Ref. [34] provides an efficient and robust regularization (this was verified by computing the binding energy of a free electron-hole pair, i.e., the hydrogenic Rydberg, with high accuracy). The details of this scheme are in Appendix B.

The resulting excitonic Schrödinger equation reads

$$\left(-\frac{\hbar^2}{2m_e} \Delta_e - \frac{\hbar^2}{2m_h} \Delta_h + V \right) \Psi = E \Psi, \quad (1)$$

where $\Delta_{e,h}$ is the Laplacian operator and $V = V_0 + V_J + V_P + V_C$. The terms of Eq. (1) only act on the electron or the hole part of the wave function, except for V_C which couples both terms. Here, Ψ and E are the 6D wave function and the corresponding total energy, respectively.

Equation (1), while straightforward conceptually, is challenging from a computational standpoint due to its 6D nature (3D in space each for electrons and holes, coupled by the

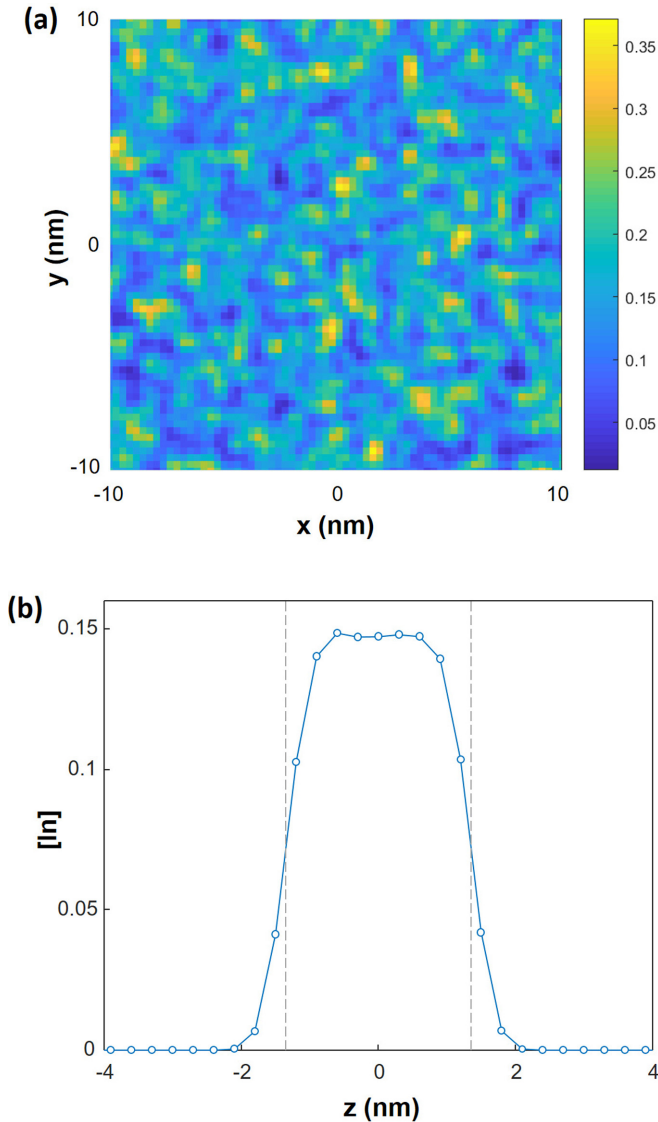


FIG. 1. Example of a configuration for an InGaN QW with $[\text{In}] = 15\%$ and $t = 2.7$ nm. (a) In-plane distribution (cross-section in the middle of the QW). (b) Composition along z (averaged along x, y), with dashed lines showing the full width at half maximum. The Gaussian averaging leads to smoothed-out interfaces.

Coulomb potential). The numerical matrix describing the Hamiltonian alone requires 5–10 GB of memory, and solving it with reasonable resources (both CPU and memory) requires a cautious approach. Additionally, Eq. (1) needs to be solved tens or hundreds of times to provide meaningful statistical averaging over disorder configurations.

In previous work, one of the present authors tackled Eq. (1) to compute the absorption spectra of InGaN QWs [28]. In that work, the absorption was computed directly by propagating the optical polarization in time; that approach was advantageous as it circumvented an explicit computation of the eigenstates of Eq. (1) [33]. However, the study of these eigenstates is precisely the object of this paper. Therefore, instead of a time propagation of the polarization, here, we solve Eq. (1) by the well-known split-operator (SO) imaginary time propagation (ITP) method (further discussed in Ap-

pendix A). ITP is widely used to compute the wave functions of numerically complex Schrödinger equations, for instance, in quantum chemistry [35,36].

We use the fourth-order ITP scheme of Ref. [37] to accelerate the convergence rate. To validate our ITP algorithm, we benchmark its result against the widespread Lancosz method (as implemented in the numerical package LAPACK), in the case of the noninteracting electron-hole problem ($V_C = 0$). In this case, Eq. (1) reduces to two decoupled 3D problems, easily solvable by the Lancosz method. The Lancosz and ITP algorithms lead to nearly identical eigenvalues and eigenvectors, with a slight shift in the particle energies (a few meVs) due to the difference in boundary conditions (namely, Dirichlet conditions with $\Psi = 0$ in the Lancosz case vs periodic boundary conditions inherent to the ITP method). When V_C is included, the Lancosz method can no longer solve Eq. (1) due to its memory scaling. On the other hand, the ITP method scales with $N^{1.5}$ (due to the fast Fourier transform steps it requires) and can typically solve Eq. (1) in 10–30 min on a modern workstation (using ~ 100 GB of memory), with a convergence of ~ 1 meV (a value sufficient for our study).

The ITP method only computes one eigenstate at a time: first the ground state, then successive higher-level states if an orthogonalization step is added to the algorithm. We implemented the higher-state calculation feature, although in most of this paper, we will focus on the properties of the ground (lowest-energy) level.

B. Wave function analysis

The solution to Eq. (1) is a 6D wave function Ψ , whose analysis is not intuitive. In practice, it is convenient to project Ψ onto more familiar wave functions of lower dimensionality, which can be plotted and interpreted. There are two textbook limiting cases where excitonic wave functions naturally lend themselves to such a factorization [38].

In the case of strong 3D confinement (e.g., an InAs quantum dot), quantum confinement dominates over the Coulomb interaction in all directions, and the wave function is well described as a nearly free electron-hole pair (i.e., with uncorrelated electron and hole motions), parameterized by real-space coordinates:

$$\Psi_{eh} = \psi_e(\mathbf{r}_e) \otimes \psi_h(\mathbf{r}_h). \quad (2)$$

In the case of a QW with no disorder (e.g., no in-plane potential), confinement in the z direction is often strong and dominates over Coulomb interaction, so that the z component of the wave function can safely be described as an independently confined electron and hole. Conversely, the in-plane movement is hydrogenoid, and the excitonic wave function can be factorized as

$$\Psi_{\text{hydro}} = \chi_e(z_e) \otimes \chi_h(z_h) \otimes \psi_{\text{abs}}(\mathbf{R}) \otimes \psi_{\text{rel}}(\mathbf{r}), \quad (3)$$

where the natural variables describing the in-plane exciton movement are its in-plane center of mass \mathbf{R} and in-plane relative position \mathbf{r} .

In our case, as the confining potential stemming from disorder and the Coulomb potential are of the same order (both in space and energy), Ψ has a hybrid nature: it cannot be factorized exactly by either of the limiting forms described

above, and some information encoded in Ψ is lost when it is approximated as a product of lower-dimension functions. Nonetheless, such factorizations are useful to visualize Ψ . Therefore, we attempt these approximate factorizations—respectively as a free electron-hole pair like Eq. (2) and as an in-plane hydrogenoid atom like Eq. (3)—and subsequently quantify how well they describe the true wave function.

For the free electron-hole pair, it is easy to compute an approximate factorization. We define an electronic pseudowave function by integrating Ψ over the hole degrees of freedom:

$$\tilde{\psi}_e^2 = \int |\Psi|^2 d^3 \mathbf{r}_h, \quad (4)$$

and likewise for $\tilde{\psi}_h$ [39]. For clarity, in the following, we call $\tilde{\psi}_{e,h}$ *interacting pseudowave functions* to distinguish them from the free-particle wave functions $\psi_{e,h}$ obtained by solving the Schrödinger equation in the absence of the Coulomb interaction.

We can then quantify how well the factorization of Eq. (2) describes Ψ by computing the overlap integral:

$$O_{eh} = \langle \Psi | \Psi_{eh} \rangle. \quad (5)$$

Here, O_{eh} is simply evaluated numerically, by integration over the modeled domain. The maximal value of O_{eh} is one and occurs if the factorization is exact.

For the hydrogenoid approximation of Eq. (3), computing the approximate factorization requires a bit more effort; the procedure is described in Appendix C. Again, we can then quantify how well Ψ_{hydro} approximates Ψ with the overlap integral:

$$O_{\text{hydro}} = \langle \Psi | \Psi_{\text{hydro}} \rangle. \quad (6)$$

Aside from these factorizations, once Ψ is obtained, various observables can be computed. Perhaps the most important is the excitonic binding energy E_B , calculated as the energy difference between the free-particle and interacting solutions: $E_B = E - E_{3D}$. With this definition, E_B is negative because the excitonic state has a lower energy than the free state; we note that, in other works, the binding energy is sometimes defined with a positive value instead. We also define the Coulomb energy $E_C = \langle \Psi | V_C | \Psi \rangle$. Note that, whereas for bulk excitons $E_B = E_C$, this is not the case here; indeed, the change in energy between free and interacting particles (E_B) is due not only to the Coulomb interaction itself (E_C) but also to the change in the potential landscape probed by the wave functions in the presence of the Coulomb interaction. Also note that the ground level of a configuration is that with the lowest total energy E , which does not especially correspond to the lowest binding energy E_B .

Another quantity of interest is the Bohr radius r_B , defined by

$$r_B^2 = \frac{1}{3} \langle \Psi | (\mathbf{r}_e - \mathbf{r}_h)^2 | \Psi \rangle. \quad (7a)$$

This definition generalizes the Bohr radius for a wave function without symmetry. The prefactor ensures that the conventional Bohr radius is recovered for a hydrogenoid wave function.

In addition to r_B , we can also compute the in-plane and vertical components of r_B by integrating over the correspond-

ing coordinates. As will be shown, for a given QW design, the vertical profile of the wave function varies very little between InGaN configurations, so that variations in r_B are caused by in-plane variations, mostly the lateral extent of the electron wave function around the hole.

C. First results

As a first example, we consider an InGaN QW with [In] = 15% and a nominal thickness $t = 2.7$ nm; these values correspond to a typical QW in a blue LED. We compute the ground state of one random InGaN configuration, both without and with the Coulomb interaction. In the absence of the Coulomb interaction, the computation simply yields the free electron and hole wave functions ψ_e, ψ_h , and the corresponding free-particle total energy $E_{3D} = E_e + E_h$. For display purposes, the probability densities in-plane and along the growth directions are computed by integrating ψ^2 along the complementary directions [i.e., along z and (x, y) , respectively].

When the Coulomb interaction is included, we compute the 6D excitonic wave function Ψ . For displaying purposes, we first factorize Ψ according to Eq. (2) to obtain interacting pseudowave functions $\tilde{\psi}_{e,h}$. We then project these along the z and (x, y) directions and compare the results to the free wave functions.

Figure 2 shows the free and interacting wave functions, in-plane and along z . Without the Coulomb interaction, the electron and hole are localized in different in-plane regions. This is because they are separated in the growth direction by the polarization fields [Fig. 2(c)] and therefore see different in-plane In distribution maps. From this observation, we conclude that it is necessary to account for the full 3D dependence of the In distribution (rather than using a separated 2D In map that would not vary along z , as had been proposed in other works) for accurate predictions. In this example, the free hole is tightly localized, and the free electron is also somewhat localized (however, electron localization is much weaker in some other configurations). Adding the Coulomb interaction has little effect on the hole wave function, as the hole is tightly localized by In fluctuations. The electron in-plane wave function, on the other hand, is pulled toward the hole by the Coulomb attraction. In the growth direction [Fig. 2(c)], both wave functions are slightly attracted toward each other due to the Coulomb interaction, but the strong confinement by the heterostructure and the polarization fields dominates.

For the configuration of Fig. 2, $E_B = -28$ meV and $E_C = -35$ meV (indeed, the Coulomb interaction pulls the electron away from its confinement region, causing a slight increase in potential energy, so that $E_B > E_C$).

We can also factorize Ψ according to Eq. (3) to explore its hydrogenoid nature. This is shown in Fig. 3. The interpretation of this figure is less straightforward and can best be understood by comparing it with the electron-hole factorization of Fig. 2(b). The center-of-mass ψ_c shows three lobes: two lobes at the peak positions of the electron and hole and one central lobe (the strongest) midway through these. This is expected, as in a classical view, the center-of-mass distribution should be peaked around $(r_e + r_h)/2$. The relative motion ψ_r is an elongated shape reminiscent of the electron wave function: indeed, as seen in Fig. 2(b), the hole is tightly localized, and

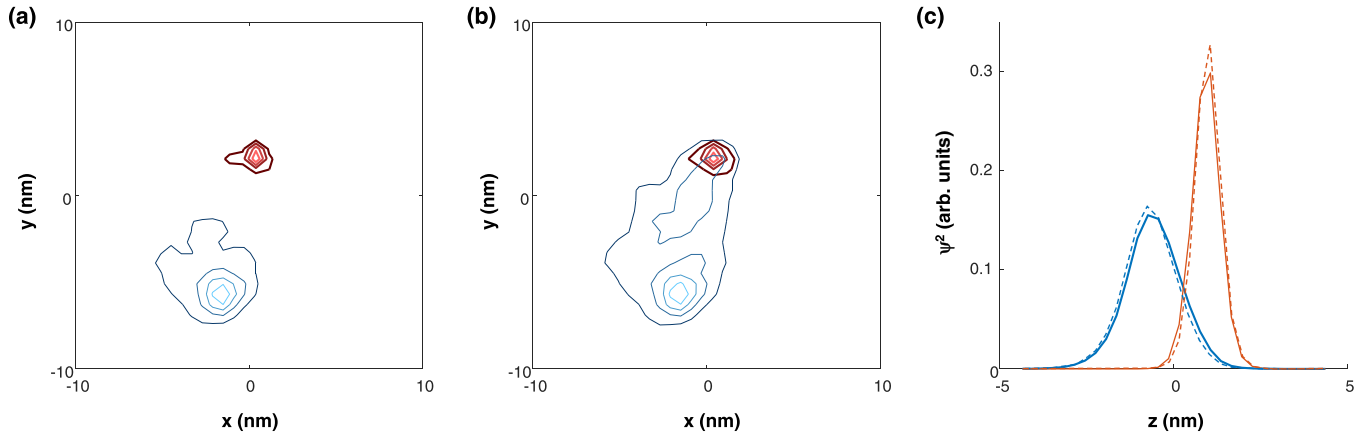


FIG. 2. Example of probability densities ψ^2 for a 2.7-nm-thick QW. (a) In-plane distribution of the noninteracting wave functions (blue/thin lines: electron; red/thick lines: hole). Here and throughout this paper, isolines mark every 20% in probability. (b) Same for interacting wave functions: the Coulomb interaction pulls the electron toward the hole. The binding energy is -28 meV. (c) Corresponding profiles along the growth direction (dashed: free; solid: interacting).

the relative motion essentially characterizes the movement of the electron around the quasipunctual hole (namely, in the negative x and y directions).

For this example, $O_{eh} = 0.99$ and $O_{hydro} = 0.52$. Therefore, Ψ is very well described by an electron-hole factorization and poorly described by a hydrogenoid approximation. As will be shown later, this result is true for many configurations, though not always. Therefore, we will generally resort to graphical representations of ψ_e and ψ_h as a way to visually study excitonic wave functions. Of course, the high value of O_{eh} does not mean that Ψ would be well described by the free (noninteracting) electron and hole wave functions. This is visible by comparing Figs. 2(a) and 2(b), where ψ_e and $\tilde{\psi}_e$ are substantially different.

The corresponding Bohr radius is $r_B = 2.2$ nm. Nonetheless, it is clear from Fig. 3(b) that the relative electron-hole motion is very anisotropic, an aspect that is not captured by r_B . In fact, if we break down the contributions to r_B along each coordinate, we find $r_x = 1$ nm, $r_y = 1.8$ nm, and $r_z = 0.6$ nm. The difference between r_x and r_y is caused by the anisotropy of the relative motion, and the low value of r_z is due to the tight vertical confinement [see Fig. 2(c)].

The focus of this paper is the exploration of the ground excitonic state. However, it can be instructive to also inspect excited levels to get insight into the various mechanisms influencing the excitonic behavior. Figure 4 shows the first three levels ($n = 1, 2, 3$) of a 2.7 nm QW (the same design as in Fig. 2 but different InGaN configuration), both in the free-particle and interacting cases. For the ground state, the behavior is like Fig. 2: the Coulomb interaction pulls the loosely localized electron wave function toward the hole; the exciton is strongly localized and hence has a high Coulomb energy. For $n = 2$, the Coulomb interaction also attracts the electron toward the hole, but it remains loosely localized, corresponding to a lower Coulomb energy. For $n = 3$, the Coulomb interaction pulls the electron from one localization region to another, which lowers the total energy; however, the electron-hole overlap is limited, so that E_C is lower.

The trends seen in the examples of Figs. 2–4 are generally true qualitatively, but significant quantitative differences occur depending on the InGaN configuration as well as the overall design of the QW. In the following section, we will therefore explore the statistical properties of excitons.

III. STATISTICAL PROPERTIES OF EXCITONS IN INGAN QWS

With the formalism of Sec. II, we investigate the impact of the QW design on the statistical properties of excitonic ground states.

As a first example, Fig. 5 shows the statistical histogram of E_B for a QW (thickness 2.7 nm, [In] = 15%) obtained from computing the ground state of 4000 InGaN configurations. The median E_B is ~ -30 meV; the distribution is rather wide, with a full width at half maximum of ~ 20 meV, showing that the random alloy configuration has a strong influence on excitonic effects. The distribution is also slightly asymmetric, with a longer tail at low energy (which gives rise to the Urbach tail in the absorption spectrum [22,28]).

It might be tempting to derive information on the absorption spectrum from Fig. 5. However, these data only pertain to the ground state of each configuration. A proper calculation of the absorption edge would require the additional computation of numerous excited states per configuration; this would require a large computational effort with the present method, which is why the time-propagation method of Refs. [28,33] is preferable for absorption computations.

In the rest of this section, for a given design (i.e., thickness and composition), we generate 100 InGaN configurations and compute the ground state for each. This is sufficient to obtain indicative statistical distributions of observables.

A. QW thickness

First, we study the impact of the QW thickness, for a constant composition [In] = 15%, a typical value for blue QWs. We consider c -plane QWs with thicknesses $t = 2, 2.7,$

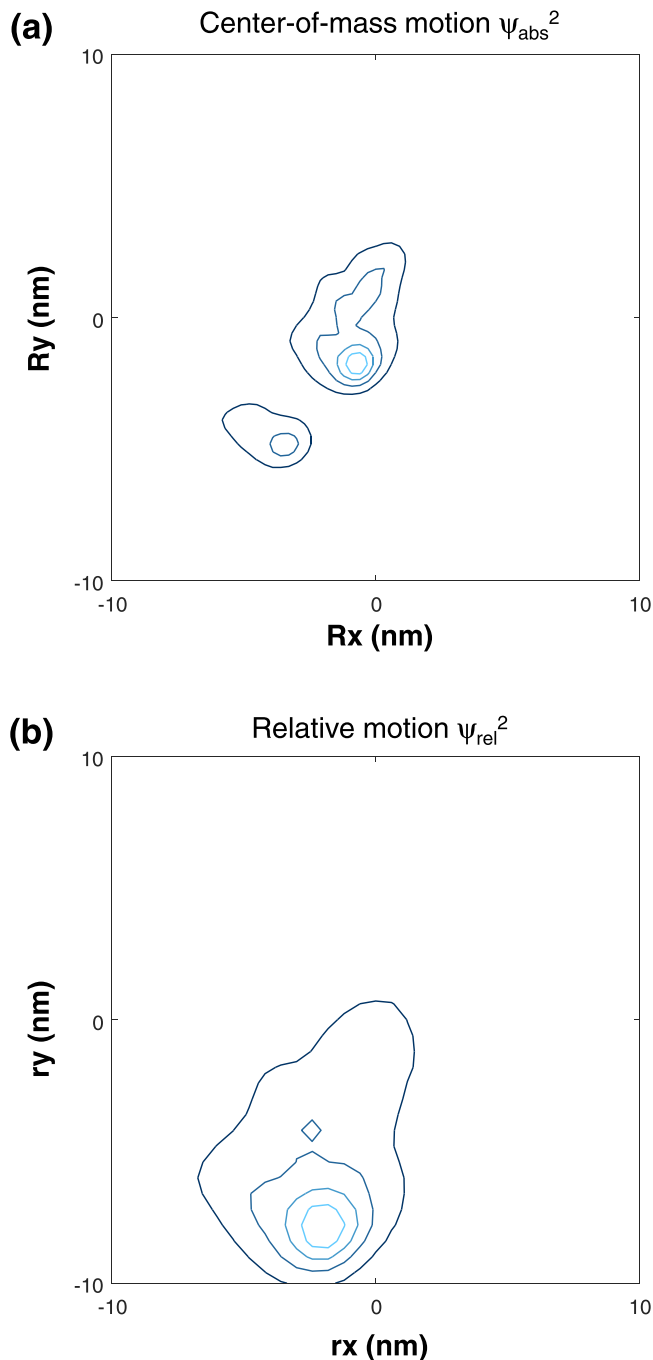


FIG. 3. Probability densities of the hydrogenoid factorization of Ψ according to Eq. (3), for the same wave function as in Fig. 2. (a) Center-of-mass motion ψ_{abs}^2 . (b) Relative motion ψ_{rel}^2 .

3.3, and 4 nm. In addition, we investigate a nonpolar (NP) QW with $t = 2$ nm. For the NP calculation, we simply turn off the polarization fields in the model. This is a simplification, which ignores the residual fields caused by local variations in In composition; nonetheless, this is suitable to study the first-order effect of NP growth, i.e., the absence of MV-scale polarization fields across the QW. Note that this NP case also approximately describes a reverse-biased c -plane QW in flat-band condition, a situation that maximizes excitonic effects, as we demonstrated experimentally in Refs. [28,40].

The QW thickness has a major impact on the binding energy, as shown in Fig. 6(a). Here, E_B is largest for the NP QW and decreases with increasing thickness for polar QWs. In each case, we show a box plot of the statistical distribution of E_B . Throughout this paper, box plots indicate the median (central horizontal line), 50% distribution (box), and 90% distribution (whiskers).

Figure 6(b) shows the corresponding total exciton energy E as a function of the QW thickness. A strong redshift is observed for thicker QWs due to the quantum-confined Stark effect. The variation in binding energy is only a second-order correction to this shift, suggesting that the thickness dependence of E_B cannot easily be observed through measurements of the total energy (e.g., in simple macroscopic optical measurements).

Figures 7–9 show corresponding examples of the pseudowave functions $\tilde{\psi}_{e,h}$ for various QW designs. In each case, six examples were chosen randomly out of the 100 calculated states. As previously discussed, this factorization of the 6D wave function as an electron-hole pair is often reasonably accurate and enables visual representations.

The NP QW has a very high binding energy, $E_B \sim 80$ meV. This is to be compared with the binding energy in bulk GaN of 23 meV. It is well known that QW confinement leads to an increased binding energy with a maximum enhancement by $4\times$ in the case of infinite confinement (i.e., for an ideal 2D exciton). The additional lateral confinement caused by fluctuations might lead to an even greater enhancement.

Here, the strong confinement, both by the InGaN/GaN heterostructure and by alloy fluctuations, leads to a median enhancement by $3.5\times$. In some configurations, disorder increases E_B . This is because electrons and holes tend to be localized in the same high-In fluctuations, leading to a further lateral confinement of the exciton and to a stronger Coulomb interaction. This is visible from the wave functions of Fig. 7: the electron wave function has a lateral extent of only a few nanometers; this is tighter than the natural extent of noninteracting electrons [Fig. 2(a)]. Figure 7 also reveals that, in a NP QW, the electron and hole are always localized in the same in-plane region. Indeed, in the absence of polarization fields, wave functions are naturally peaked near the center of the QW, so that both carriers probe the In distribution near the middle of the QW and see the same localization potential.

For polar QWs, the observed trend of decreasing E_B with thickness is expected, as the polarization field across the QW separates the electron and hole, reducing the Coulomb interaction. Overall, thin QWs retain a binding energy which is several times the thermal energy kT at room temperature, whereas in thick QWs, the binding energy is of the same order as kT .

Returning to Fig. 6, we now comment on the width of the statistical distributions. The variation in binding energy E_B depends on the QW width. It is largest for the 2 nm c -plane QW, where the energy spans the range 30–60 meV. Indeed, in this case, the competition between polarization fields (which separate the electron and hole) and the Coulomb attraction is most pronounced, leading to some configurations where one or the other effect dominates. In contrast, in thick QWs, the Coulomb interaction is a corrective effect with little variation. On the other hand, the total energy E always has a wide

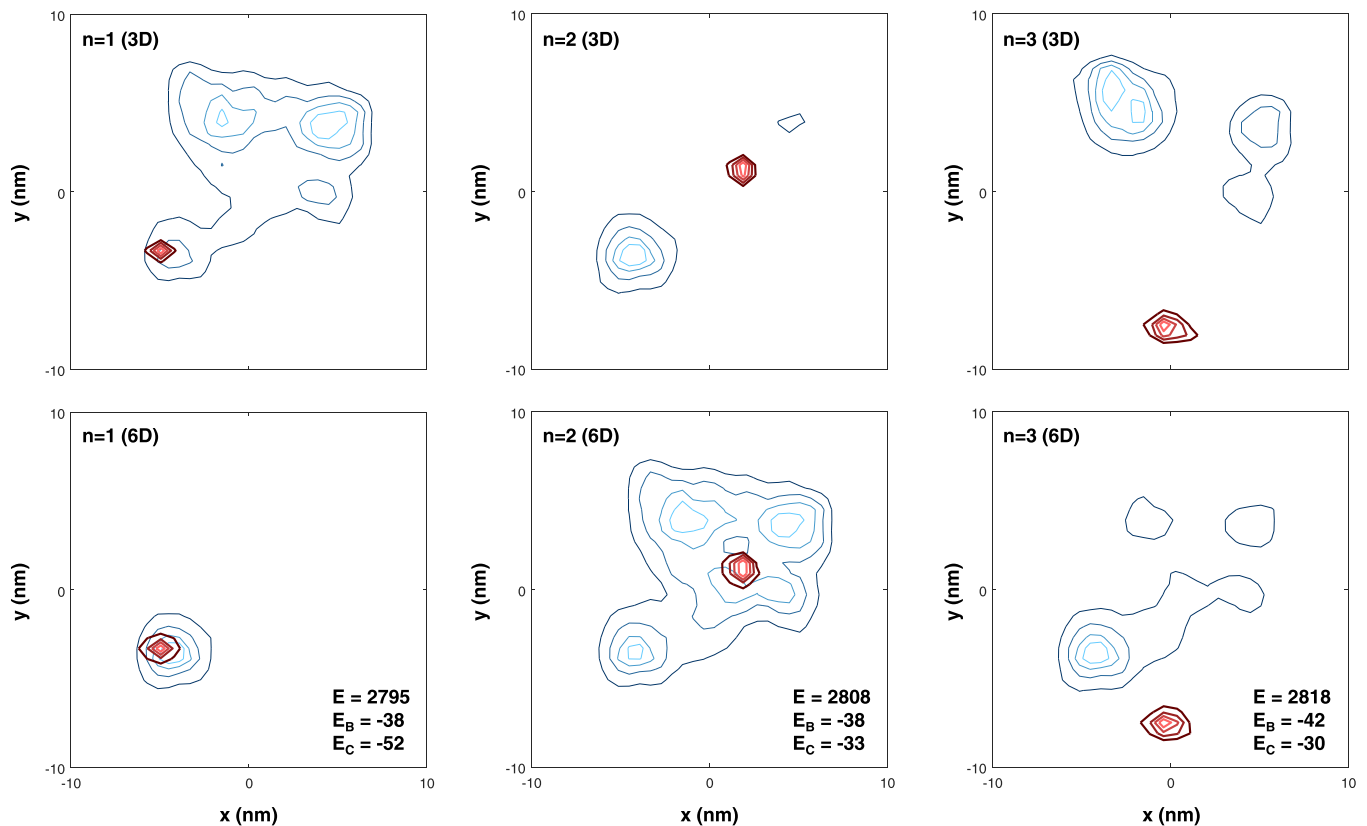


FIG. 4. Probability densities ψ^2 for the first three levels of a 2.7-nm-thick QW with $[\text{In}] = 15\%$ (top) in the absence of the Coulomb interaction and (bottom) with Coulomb interaction. For each level, three energies are indicated (in meVs): the total energy E , the binding energy E_B , and the Coulomb energy E_C .

distribution because it is affected by alloy disorder regardless of Coulomb interaction.

Examining the wave functions of Figs. 7–9 shows that, as the QW thickness increases and E_B decreases, electron wave functions become more spread spatially around the hole (because the Coulomb interaction becomes weaker). Note that, while a higher E_B often corresponds to electron and hole wave functions localized closely together in space, this is not always true: as already mentioned (and illustrated in Fig. 4), this is because E_B is caused not only by the Coulomb energy E_C but also by the change in the energy landscape probed by the wave function.

Another way to assess the spatial extent of wave functions is through the Bohr radius r_B ; this characterizes the relative distance between electron and hole rather than the individual extent of each particle. Figure 10(a) shows that r_B is smallest for the NP QW and increases with thickness for polar QWs. Notice that these variations are not evident from direct visual inspection of Figs. 8 and 9, which shows the necessity of statistical assessments. There is a substantial scatter in the statistical distribution of r_B . As shown in Fig. 10(a), this is caused by variations in the in-plane component of r_B . In contrast, the vertical component is dominated by the polarization field-induced separation and barely depends on the configuration. Figure 10(b) shows the correlation between the radius and binding energy. In general, a smaller radius corresponds to a higher binding energy, as expected since the better overlap of the localized electron and hole corresponds

to a stronger Coulomb interaction [41]. The correlation is especially pronounced for thin and NP QWs, where the interaction is strongest.

We conclude this section with an examination of the nature of the 6D wave function and whether it can be factorized as an electron-hole pair [Eq. (2)] or as a hydrogenoid atom [Eq. (3)]. Figure 11 shows the value of O_{eh} and O_{hydro} for QWs of varying thickness (with ten configurations calculated for each thickness). For thick QWs, O_{eh} is close to unity, while O_{hydro} is low, indicating that the wave functions are well described as weakly interacting particles, as already seen in the example of Fig. 2. For thinner QWs, O_{eh} decreases, while O_{hydro} increases, and in the NP case, some configurations have a similar value (~ 0.8) for both quantities. This indicates that, as the Coulomb interaction increases, the wave function acquires a hybrid nature, which is neither simply hydrogenoid nor electron-hole-like.

To help interpret these results, Fig. 12 shows sketches of excitonic wave functions in a few simplified cases. If the confinement domain is large compared with the Bohr radius as in (a), the exciton retains a hydrogenoid nature ($O_{hydro} \sim 1$), with an absolute (or center-of-mass) movement across the domain; this case is not realized in InGaN compounds, where the typical scale of random alloy fluctuations is too small. If the confinement is strong, with the same confinement domain for electrons and holes as in (b), the exciton is strongly interacting but has no center-of-mass motion; this occurs in NP QWs. In the intermediate regime (c) where the localization domains

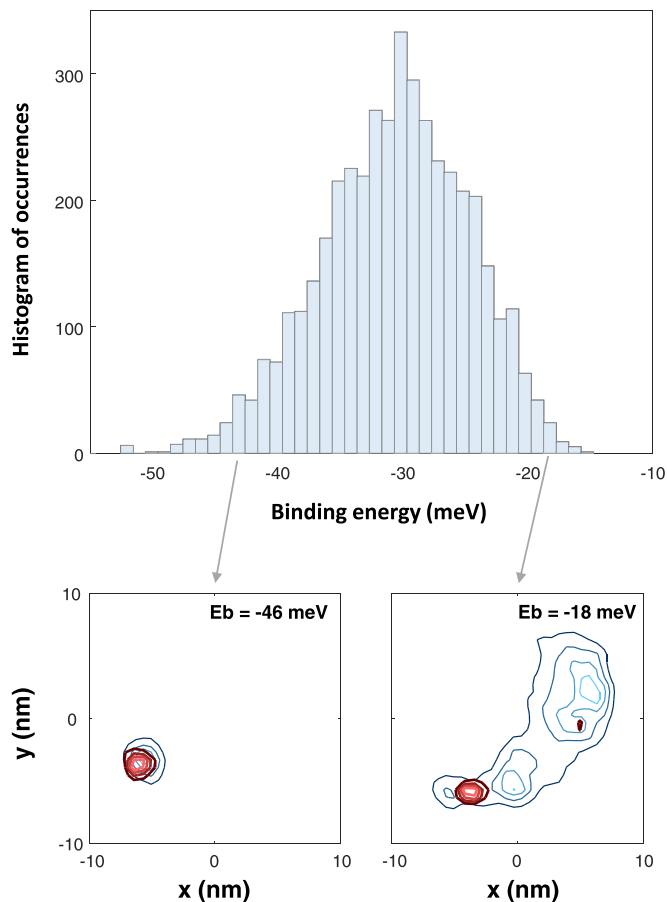


FIG. 5. Statistical histogram of E_B for a 2.7-nm-thick QW, derived from 4000 configurations. The wave functions corresponding to two configurations are shown: a tightly bound exciton ($E_B = -46$ meV), for which the electron and hole components strongly overlap, and a loosely bound exciton ($E_B = -18$ meV), for which the electron component is weakly localized and does not overlap much with the hole component.

are strong and overlapping, the excitonic wave function has a hybrid nature, somewhat single-particle-like in some regions of space and with a true 6D nature in others; this occurs in thin polar QWs. If the confinement is strong, with small domains separated in space as in (d), the exciton is essentially a free (uncorrelated) electron-hole pair with a Coulomb correction ($O_{eh} \sim 1$); this occurs in thick QWs.

B. QW composition

The same calculations are then repeated for QWs with compositions in the range $[\text{In}] = 5\text{--}25\%$ (spanning the violet-to-green range). The results are shown in Fig. 13, which represents a useful map of the world of the binding energy for various QW designs.

An increased In composition causes competing effects: larger In fluctuations (which lead to stronger localization and hence more Coulomb interaction) and stronger polarization fields (which separate electrons and hole, reducing their interaction). This competition is apparent in the trends of Fig. 13.

For the NP QW, the binding energy becomes larger with $[\text{In}]$ due to the stronger lateral confinement at fluctuations.

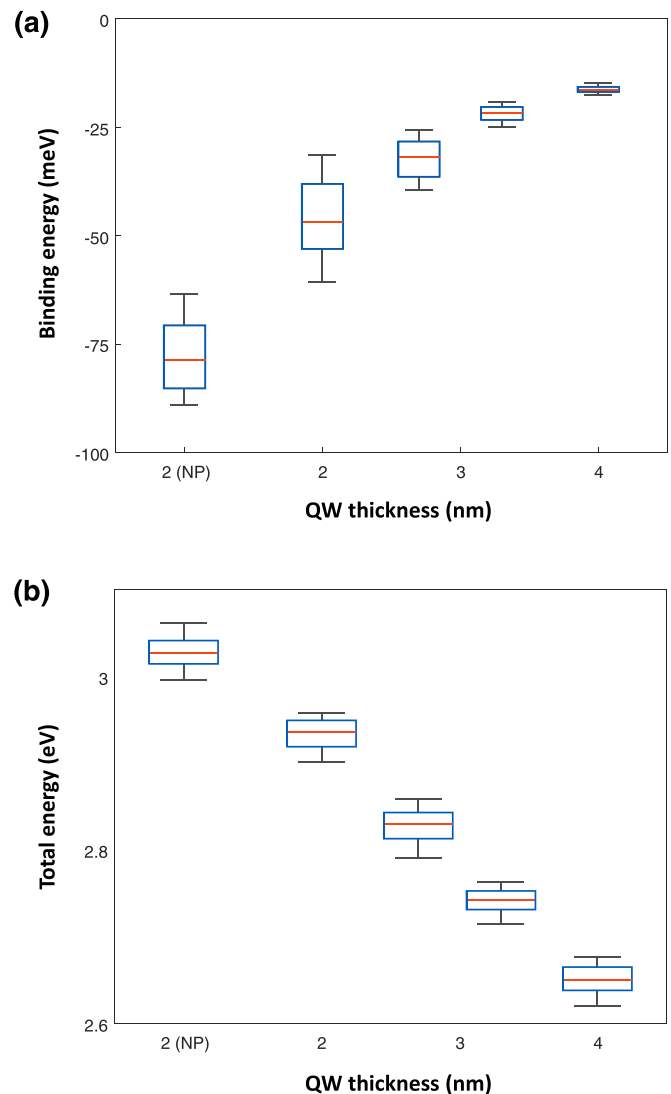


FIG. 6. Statistics of ground state energy vs QW thickness. (a) Binding energy. The body of the box shows the 50% probability; the whiskers the 90% probability; the horizontal line is the median. E_B decreases for thicker QWs due to the field-induced separation of electrons and holes. (b) Total energy E . This quantity strongly decreases for thicker QWs due to the larger redshift induced by the quantum confined Stark effect.

In the absence of polarization fields, this is the only relevant effect. The statistical distribution of E_B is wide, regardless of the composition.

For the polar QWs, on the other hand, the effect of polarization fields dominates, and E_B becomes smaller with higher $[\text{In}]$.

For thin polar QWs (2 nm), the statistical distribution of E_B is broad, regardless of the composition. Increasing $[\text{In}]$ leads to a modest reduction in E_B because the polarization fields have a moderate effect. For thick polar QWs on the other hand, the composition has a strong influence on the excitonic behavior: at low In composition, the weak polarization fields allow a large electron-hole overlap and a significant Coulomb interaction, with wide statistical variations depending on the configuration; at high In composition, however,

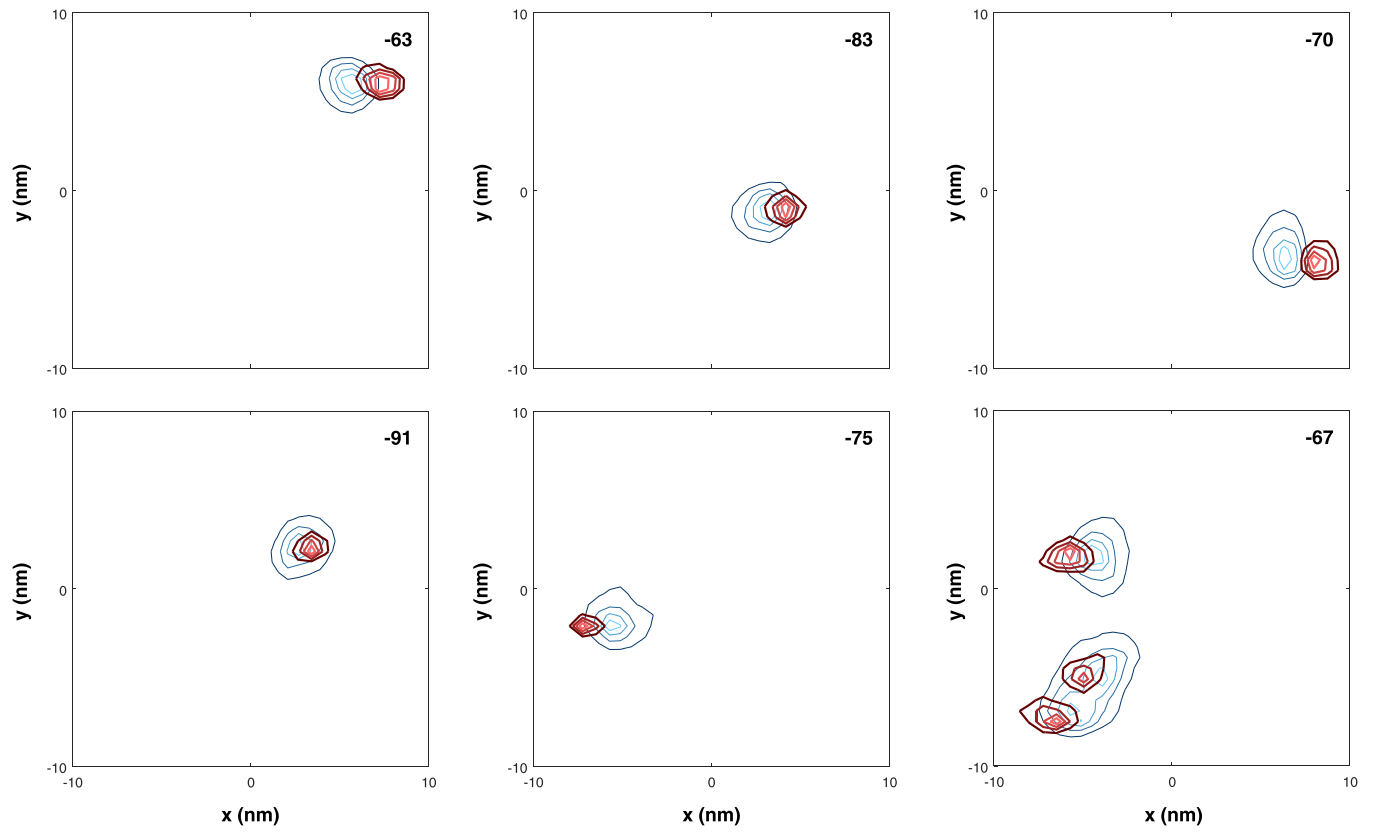


FIG. 7. Examples of in-plane wave functions ψ^2 for six configurations of a 2 nm nonpolar QW (blue: electron; red: hole). The binding energy (in meVs) is shown in the upper-right corner.

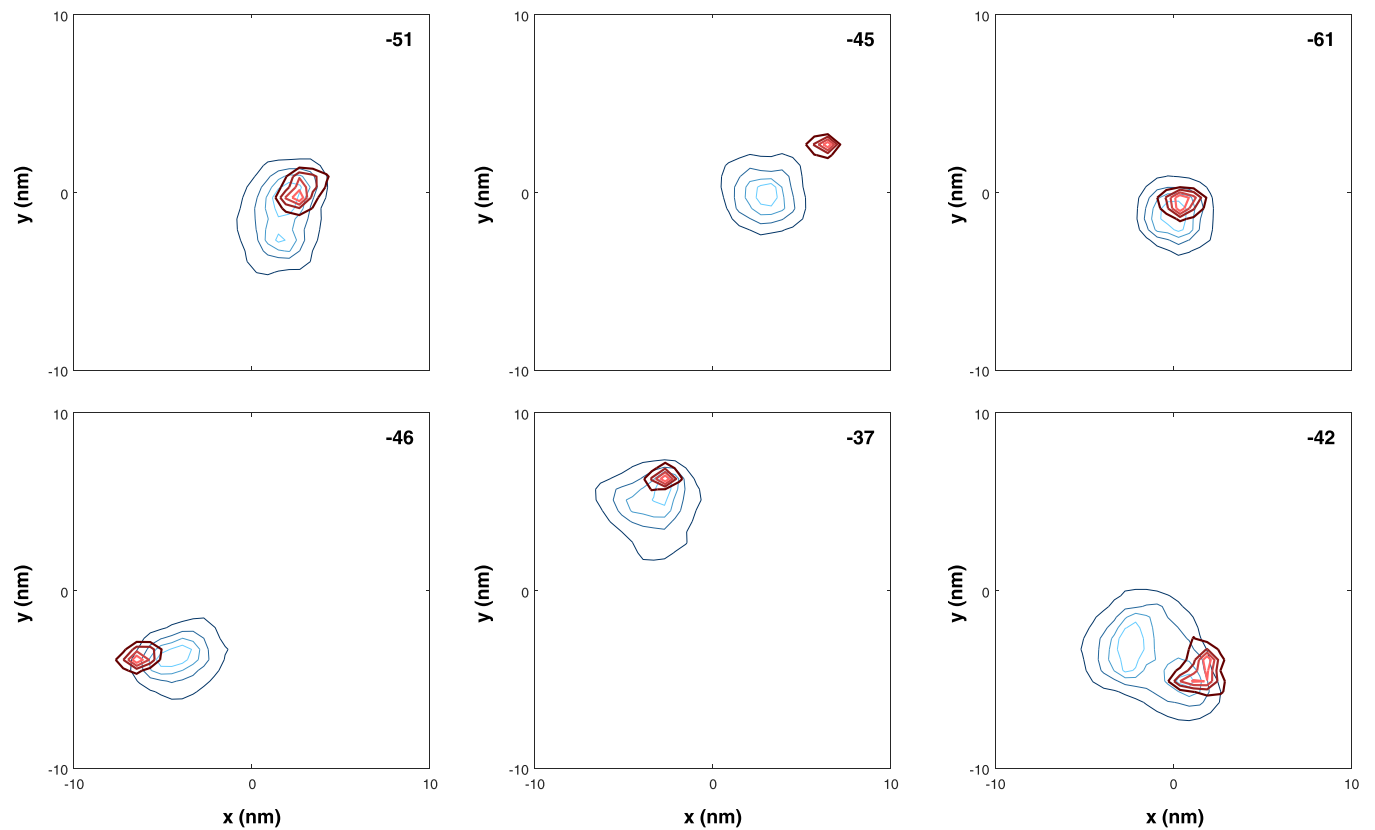


FIG. 8. Examples of wave functions for a 2 nm polar QW (see caption of Fig. 7 for details).

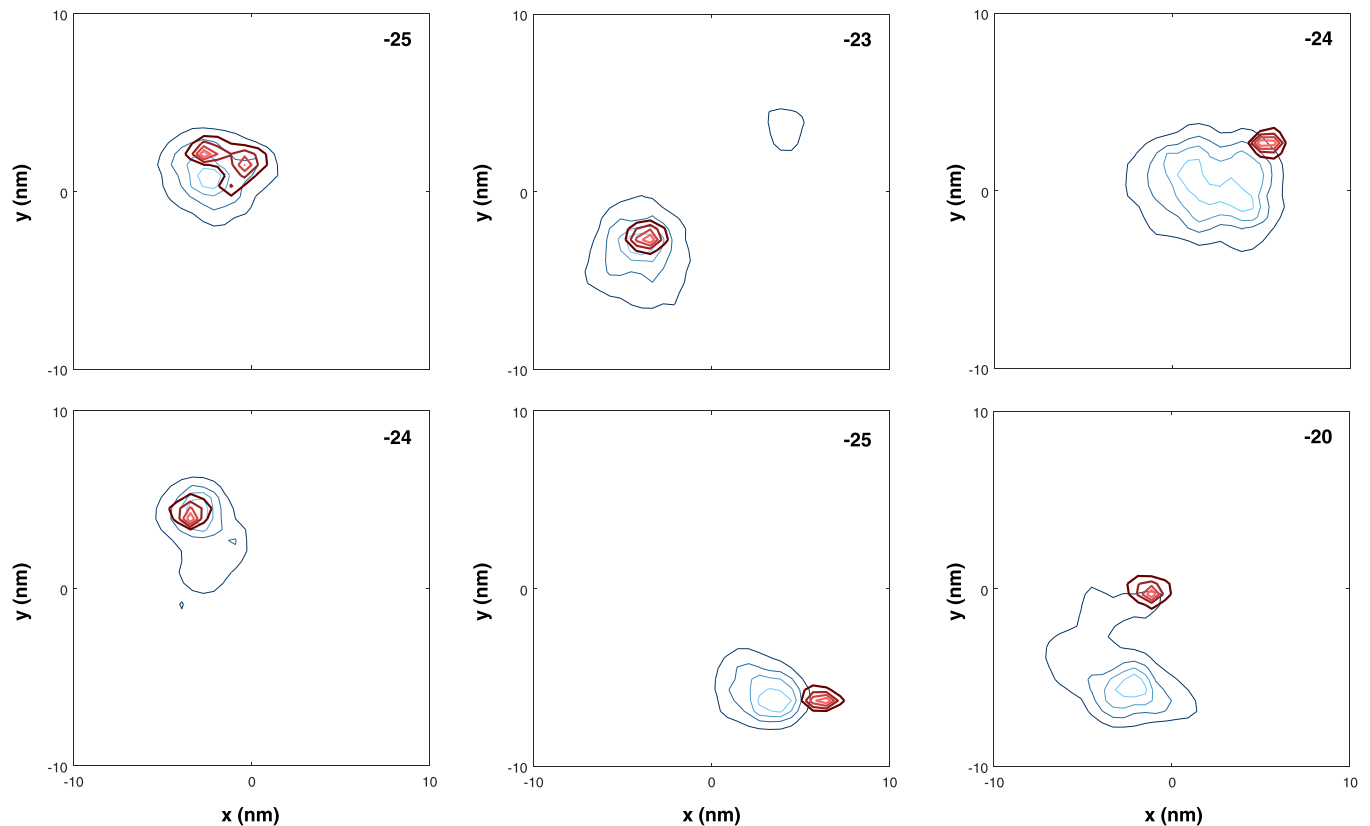


FIG. 9. Examples of wave functions for a 3.3 nm polar QW (see caption of Fig. 7 for details).

polarization-field-induced separation of electrons and holes dominates, and the Coulomb interaction becomes weak and nearly independent of the configuration.

Interestingly, for the lowest In composition, E_B becomes similar regardless of the QW thickness. This is because the polarization fields become weak, and the QW thickness becomes less relevant. In addition, E_B diminishes well below the 2D limit of $4\times$ the bulk value; indeed, for low In content, the confinement by the heterostructure becomes weak, and the excitons lose their bidimensional nature. Our model is not suited for very low In compositions, but for even lower values of [In], we expect E_B to converge for all QW thicknesses.

A noteworthy implication of Fig. 13 is that the average value of E_B can be tailored from near zero to nearly 100 meV by selecting an appropriate QW design. This may be valuable in applications where a specific binding energy is desirable.

IV. EXCITON SCREENING

All the previous calculations assume a full Coulomb interaction. In the presence of free carriers (i.e., of an electron-hole plasma), the Coulomb interaction is progressively screened. We investigate this effect with a screened Coulomb potential V_S in the RPA approximation (also known as the Yukawa

potential) [28,42]:

$$V_S(r) = V_C(r) \exp(-\kappa r), \quad (8a)$$

$$\kappa^2 = \frac{2e^2 n}{\epsilon_0 \epsilon_r k_B T}, \quad (8b)$$

with n the free carrier density. Hence, κ is the inverse of the Thomas-Fermi screening length.

In addition to the screening of V_C , we include the screening of the polarization fields by free charges. This is accomplished by a conventional Poisson-Schrödinger loop. Polarization screening is only meaningful at the highest carrier densities $n > 10^{19} \text{ cm}^{-3}$.

We consider a QW of thickness 2.7 nm and composition [In] = 15%. Figure 14(a) shows the screening of E_B for 10 configurations. In each case, the excitonic interaction is significantly reduced for n in the range 10^{17} – 10^{18} cm^{-3} (when $1/\kappa$ becomes commensurate with the Bohr radius), and E_B becomes very low for $n \geq 1 \times 10^{19}$ to $3 \times 10^{19} \text{ cm}^{-3}$.

As a reference point, Fig. 14(a) also shows the screening of E_B for a bulk exciton in GaN. In this case, there is no potential from the heterostructure, and only the screened Coulomb potential is present. In the bulk case, E_B vanishes for a finite carrier density $n = 10^{18} \text{ cm}^{-3}$. This is a property of the Yukawa potential: above a critical value of the screening length, the Schrödinger equation no longer admits a bound state.

The behavior in the case of disorder stands in contrast to this: E_B tends toward zero for high values of n but always

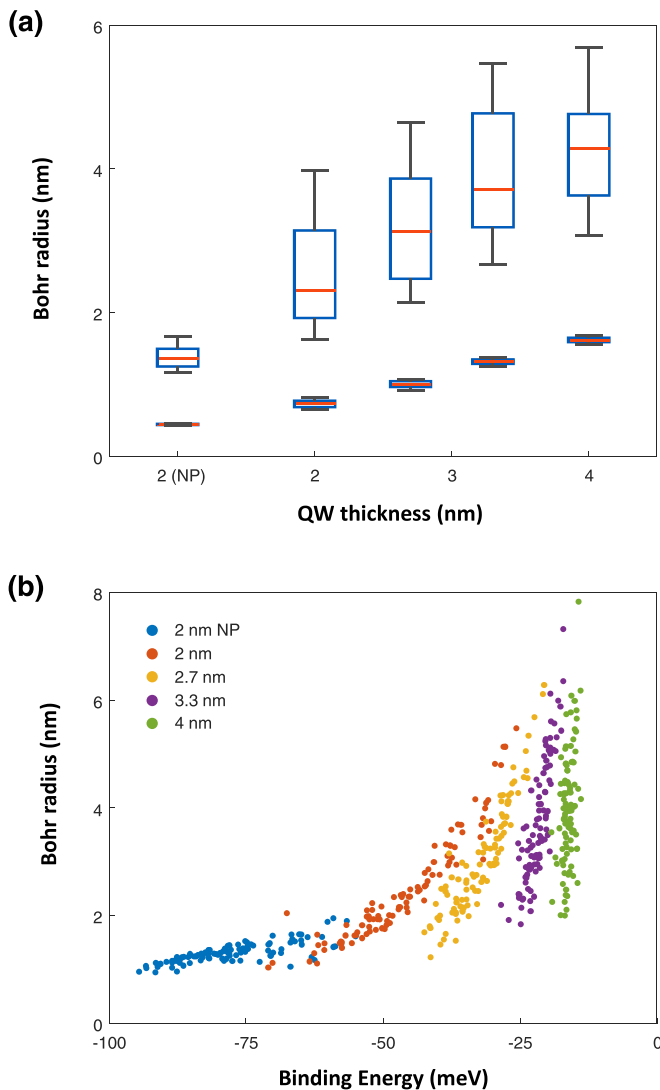


FIG. 10. (a) Box plots of the Bohr radius as a function of QW thickness (top boxes: total radius r_B ; bottom boxes: vertical component of the radius r_{Bz}). The vertical component scales with the QW thickness and has a narrow statistical distribution. The large distribution of r_B is caused by variations in the in-plane profile. (b) Correlation between the Bohr radius and binding energy.

retains a finite value. This is because the electron and hole wave functions always remain localized by disorder and can always form a (weakly) bound pair in the presence of screened Coulomb interaction.

The screening behavior of Fig. 14(a) resembles a sigmoid. Based on this observation, we seek an analytical function that approximately describes the screening. Figure 14(b) shows the same screening data, normalized to unity at low density. Despite some scatter, the overall screening behavior is similar for all configurations. Empirically, we find an acceptable fit to these data by the following function:

$$\frac{1}{1 + (n/n^*)^\alpha}, \quad (9)$$

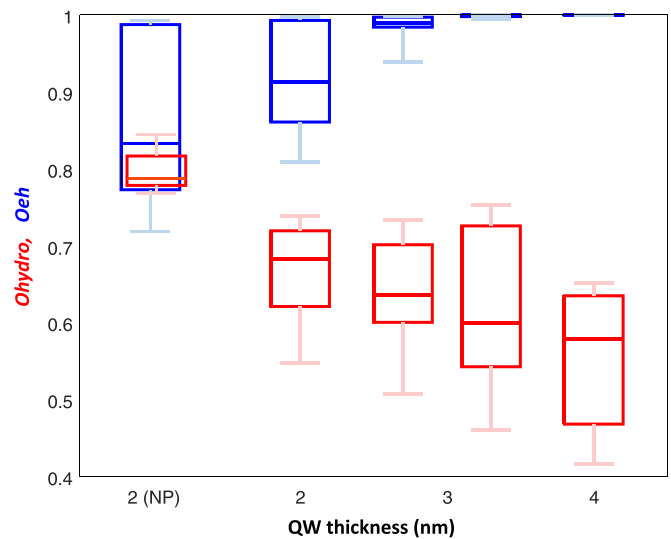


FIG. 11. Statistics of the wave function factorizations O_{eh} and O_{hydro} as a function of QW thickness. For thick QWs, $O_{eh} \sim 1$ and O_{hydro} is low, indicating a free-particle nature. For thin QWs and especially for nonpolar (NP) QWs, the wave function acquires a hybrid nature.

with $n^* \sim 2 \times 10^{17} \text{ cm}^{-3}$ and $\alpha = \frac{2}{3}$. This approximation may be useful for describing screening effects without solving the full numerical problem.

Screening calculations were repeated for various QW designs: NP 2-nm-thick QW and polar QWs with thicknesses 2, 2.7, 3.3, and 4 nm, all with 15% In. Figure 15(a) shows the normalized binding energy [the same quantity as in Fig. 14(b)] in each case. All the curves share the same sigmoidal shape, but the onset of screening varies; it occurs at low carrier density in thick QWs where excitonic binding is weak and at high density in the NP QW with the strongest excitonic effects. The empirical function of Eq. (9) fits all curves well, with a same value of $\alpha = \frac{2}{3}$. The characteristic screening density n^* corresponds to the point where the normalized binding energy equals 0.5; it is $< 10^{17} \text{ cm}^{-3}$ for the 4 nm QWs and slightly $> 10^{18} \text{ cm}^{-3}$ for the NP QW.

These values of n^* should be compared with two other typical densities that govern recombination physics: the density for screening of the polarization fields $n_{polar} \sim 5 \times 10^{18} \text{ cm}^{-3}$ [28], and the phase-space-filling density at which the carrier statistics become degenerate $n_{PSF} \sim 10^{19} \text{ cm}^{-3}$ [43]. Therefore, excitonic effects are expected to be screened before the onset of these other carrier-dependent phenomena.

Once the screening behavior is known, the excitonic population can be investigated. The equilibrium population is conventionally computed with the Saha equation, a mass-action law that relates the free and excitonic populations [16,44]. The Saha equation is expressed between discrete energy levels, in contrast to the band of excitonic states caused by disorder. For simplicity, we nonetheless employ the conventional Saha expression, using the median value of the binding energy. For a 2D system, the Saha equation reads

$$n_{ex} = n_{free}^2/n_Q, \quad (10)$$

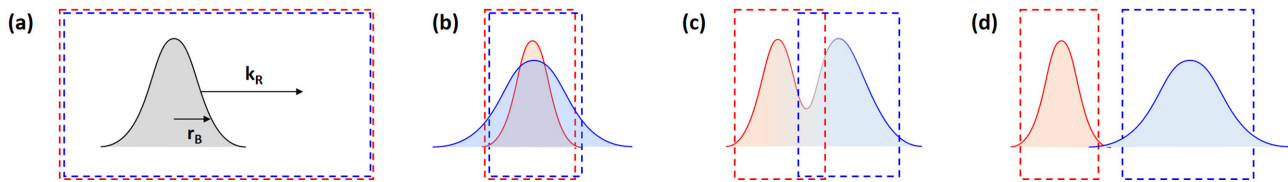


FIG. 12. Sketches of excitonic wave functions in various confinement cases: (a) The confinement domain is much larger than the Bohr radius r_B , the exciton is hydrogenoid with movement k_R . (b) The confinement domain is strong and is the same for electrons and holes. (c) Intermediate case where confinement domains are strong and partially overlapping. (d) The confinement domains are strong and separated, yielding nearly free particles. Dashed lines: confinement domain. Blue: electron; red: holes; gray: both carriers.

with $n_Q = m_r k_B T / \{2\pi \hbar^2 [\exp(E_B/k_B T) - 1]\}$, n_{ex} the excitonic density, and n_{free} the free density of electrons (and holes). The total carrier density is $n = n_{ex} + n_{free}$. All these are 2D densities, related to 3D densities by $n_{3D} = n_{2D}/t$, with t the QW thickness. The binding energy E_B depends on n_{free} , as shown in Fig. 15(a).

Figure 15(b) shows the excitonic fraction n_{ex}/n obtained from Eq. (10). At first, the population grows quadratically with n , before saturating and decreasing due to screening. In the NP QW, a substantial fraction of the carriers can be in the excitonic phase at high density. On the other hand, for polar QWs of typical thicknesses (2.7 nm and thicker), most carriers (90% or more) remain free at all densities.

This suggests that no significant excitonic populations should be present in commercial LEDs under typical operating conditions. Indeed, these LEDs employ *c*-plane QWs, with thicknesses ~ 3 nm and are usually driven at densities well above $> 10^{18} \text{ cm}^{-3}$. This is in agreement with the findings of Ref. [28], where one of the present authors concluded that the influence of the Coulomb interaction on radiative properties was caused by Coulomb enhancement of the coupling between free carriers and photons rather than by excitonic

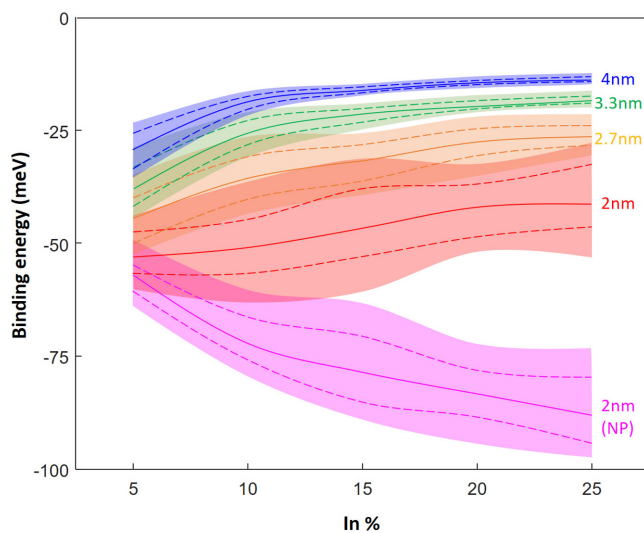


FIG. 13. Binding energy for various In compositions and QW thicknesses. For each QW thickness, the solid line shows the median; the dashed lines show the range containing 50% of values; the shaded region shows the range containing 90% of values. The slight waviness of some curves is attributed to the moderate number of computed states (100 in each computation).

populations. Our predictions can also be compared with the measurements of Ref. [15], where the excitonic population was estimated from terahertz measurements: in that study, the trend for a thin QW looks somewhat like the present predictions. However, the measurements also find nearly identical

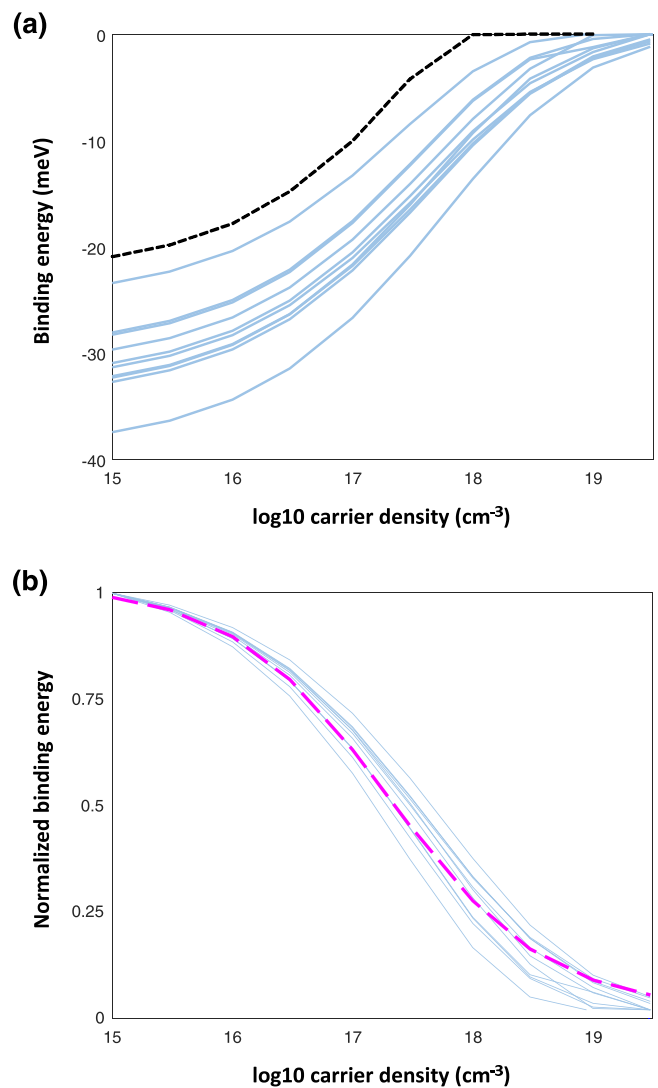


FIG. 14. (a) Screening of the binding energy as a function of the free carrier density. Each line is an individual configuration. The dashed line corresponds to a bulk GaN exciton. (b) Same as (a), with each curve normalized to unity at low carrier density. The dashed line is a fit by an analytic function, as described in the text.

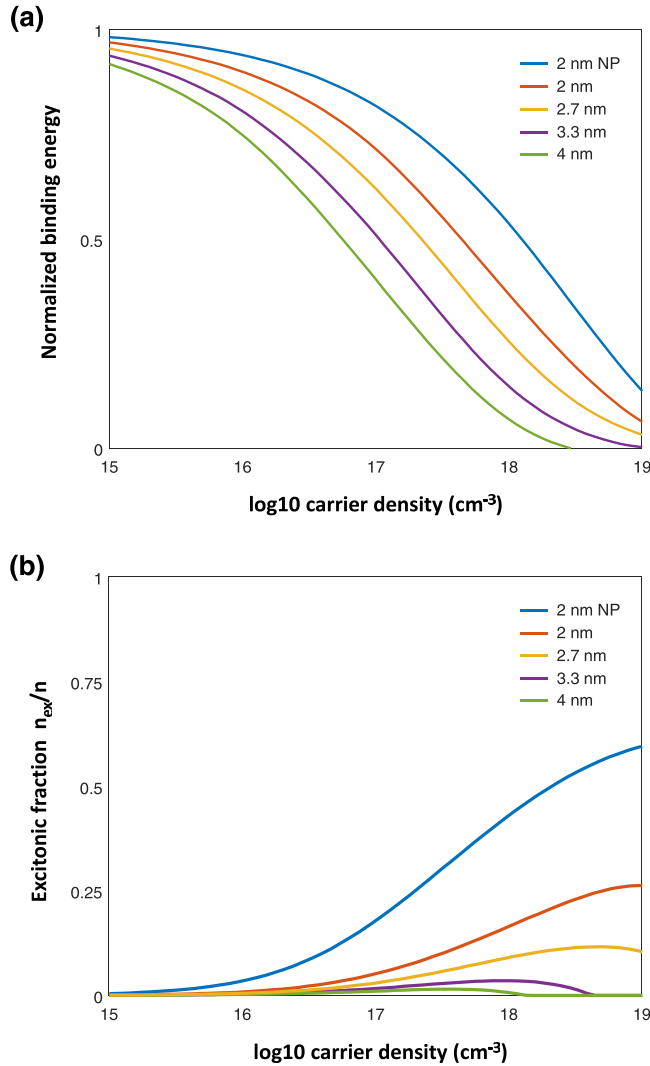


FIG. 15. (a) Normalized screening of the binding energy with carrier density, for various QW designs. All QWs have 15% In. In thicker QWs, excitons are screened at lower density. (b) Fraction of carriers in the excitonic phase vs the total carrier density, according to the Saha equation.

excitonic populations regardless of the QW thickness; this finding is difficult to reconcile with the unavoidable decrease in binding energy for thick QWs.

V. AN APPROXIMATION WITH REDUCED NUMERICAL COMPLEXITY

Throughout this paper, the excitonic wave function was obtained by directly solving the 6D Schrödinger equation Eq. (1). While a modern workstation can tackle this problem, a reduction in complexity would be desirable. For instance, it could help compute a large number of states more rapidly (i.e., for integration in a Poisson-Schrödinger device solver) or to tackle future, more demanding problems such as the computation of biexcitonic wave functions, a 12-dimensional (12D) problem which cannot be solved by brute computational force.

One might consider solving Eq. (1) with a variational approach. However, given the complex shape of the in-plane wave functions shown in Figs. 7–9, it is not clear what kind of parameterization would be suitable. This calls for a different strategy to reduce the complexity of the numerical problem.

In this section, we present an approximate solution of Eq. (1) which retains excellent accuracy.

Our approach is based on the observation that the confinement in the epitaxial direction (z) is very strong, both for electrons and holes. Therefore, one may wonder if the exact solution can be factorized into a separable form, where variations along (z) and (x, y) are separated. We now investigate this, starting with the free-particle problem for simplicity.

A. Approximation of the free-particle problem

We consider the 3D problem of the free electron (the approach for holes is identical) in a potential $V(x, y, z)$. We seek a solution of the form $\psi = \chi(z) \times \phi(x, y)$, corresponding to a decomposition of the potential as $V = U(z) + W(x, y)$. Since the average confinement along z does not depend much on composition fluctuations, we define as a first approximation to U an effective potential along z :

$$U_0(z) = \frac{1}{L_x L_y} \int V dx dy. \quad (11)$$

We solve the resulting one-dimensional (1D) Schrödinger equation $(-\hbar^2 \Delta_z / 2m + U_0)\chi_0 = E_{0,z}\chi_0$, where χ_0 is a first approximation of χ . We then use χ_0 to define the average lateral potential seen by the electron as

$$W_0(x, y) = \frac{1}{L_z} \int (V - U_0)\chi_0^2 dz. \quad (12)$$

In other words, W_0 is the remaining part of V (after the vertical component U_0 is subtracted), averaged over the vertical probability density χ_0^2 . We solve the corresponding 2D equation $(-\hbar^2 \Delta_{xy} / 2m + W_0)\phi_0 = E_{0,xy}\phi_0$, where ϕ_0 is a first approximation of ϕ .

Using ϕ_0 , we then refine our approximation of the vertical potential:

$$U_1(z) = \frac{1}{L_x L_y} \int V |\phi_0|^2 dx dy. \quad (13)$$

Compared with Eq. (11), this new estimate considers how ϕ_0 probes the potential V .

We subsequently compute the corresponding wave function χ_1 , use it to define an in-plane potential W_1 and the corresponding wave function ϕ_1 , and keep iterating this process until the wave functions and energies converge. Upon convergence, the potentials U and W are therefore averages of V , weighed in-plane and in the vertical direction by the squared wave function.

The iterative Schrödinger equations are solved by the same ITP algorithm as in Sec. II. In practice, ~ 3 – 4 iterations are sufficient for the energy to converge within < 1 meV. The total energy is $EE = E_z + E_{xy}$.

This approach produces an excellent approximation of the electron wave function. We quantify this by two metrics: the energy difference $E - EE$, and the wave function overlap between the exact and approximate solutions (i.e., between

ψ and $\chi \times \varphi$). We find that the energy is systematically overestimated by a small constant shift of a few meVs (a small error compared with the total energy E , on the scale of several hundred meVs), and the overlap is typically on the order of 99%, indicating that the exact and approximate wave functions are nearly identical.

Equally good agreement is found for the free hole problem. In summary, the 3D free-particle problem can efficiently be factorized into 1D and 2D problems.

$$U_p = \frac{1}{(L_x L_y)^2} \int V |\varphi_{p-1}^2| dx_e dy_e dx_h dy_h, \quad (14)$$

$$\left(-\frac{\hbar^2}{2m_e} \Delta_{z_e} - \frac{\hbar^2}{2m_h} \Delta_{z_h} + U_p \right) \chi_p = E_{z,p} \chi_p, \quad (15)$$

$$W_p = \frac{1}{L_z^2} \int (V - U_p) |\chi_p^2| dz_e dz_h, \quad (16)$$

$$\left(-\frac{\hbar^2}{2m_e} \Delta_{x_e, y_e} - \frac{\hbar^2}{2m_h} \Delta_{x_h, y_h} + W_p \right) \varphi_p = E_{xy,p} \varphi_p. \quad (17)$$

Thus, the 6D problem is separated into 2D and four-dimensional (4D) problems, which again are solved by the ITP algorithm. In the first iteration of Eq. (14), we use a uniform trial function $\varphi_{-1} = 1$ (modulo a normalization factor) to seed the iterative loop.

The same excellent agreement is found as in the free-particle case. The total energy is systematically overestimated by a small amount ~ 10 meV. The overlap integral between the exact and approximate wave functions is again on the order of 0.99. Figure 16 shows the correlation between the energy of the exact and approximate solutions, for various QW designs.

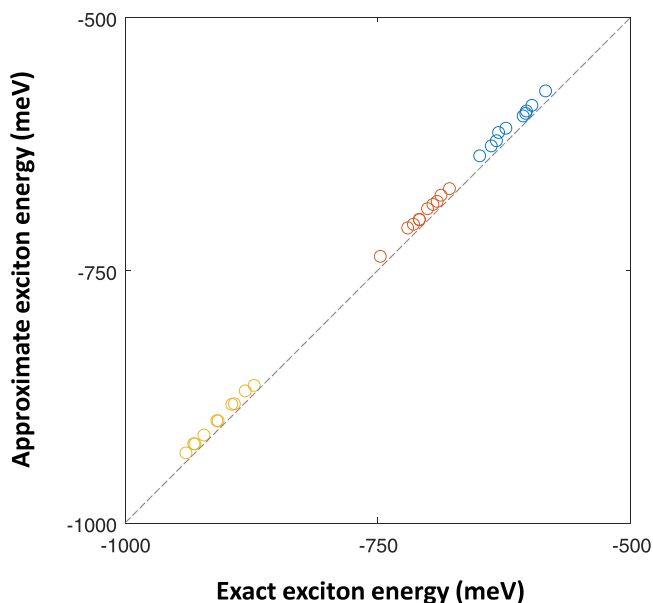


FIG. 16. Correlation between the binding energies calculated with the exact and approximate methods. Each circle is an individual configuration [blue/red/yellow: 4/2.7/2 nm QW thickness]. The dashed line indicates a perfect correlation. The approximate energies are systematically shifted by ~ 10 meV.

B. Approximation of the excitonic problem

The generalization of this method to the 6D exciton problem is straightforward. We seek a solution $\Psi = \chi(z_e, z_h) \times \varphi(x_e, y_e, x_h, y_h)$, corresponding to a decomposition of the potential as $V = U(z_e, z_h) + W(x_e, y_e, x_h, y_h)$. We define the potentials and wave functions iteratively at step p as follows:

In summary, this approximation is capable of predicting the excitonic wave functions very accurately, while reducing the dimensionality of the problem from 6D to 4D. This method enables the computation of an excitonic wave function in ~ 1 min.

Further, we anticipate that it may enable the future calculation of the biexcitonic wave function by reducing it to an eight-dimension problem, obviously still a very complex problem but less daunting than the full-fledged 12D equation.

VI. PROSPECTS FOR EXPERIMENTS: PROBING EXCITONS IN III-NITRIDE COMPOUNDS

We conclude this study with a discussion of existing experiments to probe excitonic effects and prospects for future experiments. A key challenge is to probe not only the effect of localization but how it specifically affects excitons, as opposed to free particles.

We note that, as we focus on localization caused by random alloy disorder, we ignore the additional effect of crystal defects such as dislocations. The spatial distribution of potentials around a dislocation can be complex and has been studied, e.g., in Ref. [45]. However, the density of threading dislocations in conventional GaN structures (on the order of 10^8 cm^{-2}) is sparse when compared with the scales we study here. Namely, the density of localization potentials from random alloy fluctuations, as well as exciton Bohr radius, are a few nanometers. Therefore, we expect that the physics of localization in the QW are dominated by random alloy effects and are appropriately described by our model. Further discussion of the various scales over which localization may occur can be found in Ref. [46].

A. Macroscopic measurements

To date, there have only been a few observations of exciton effects in InGaN alloys. One limitation of macroscopic

absorption or luminescence measurements is that they only probe spatially averaged excitonic effects.

Absorption measurements in QWs under reverse bias (in flat-band conditions) have shown clear excitonic peaks at room temperature, across a wide range of composition [28,40]; similar measurements in bulk materials have also shown excitonic resonances at low temperature, though they tend to get smeared out at high In content (possibly due to a degradation in the material quality) [47,48]. These measurements, however, are not easily related to the present analysis, as they probe many states: ground and excited exciton states and continuum states at different configurations. In contrast, in this paper, we compute the ground state of each configuration. Instead, a more convenient framework to model macroscopic experiments is to directly compute the overall optical response of the disordered system (without explicitly computing individual solutions of the Schrödinger equation). This was done by one of the authors in Ref. [28], where it was shown that the rather broad excitonic peak is in fact caused by a multitude of single excitonic lines, broadened by disorder.

To further probe the properties of low-energy excitonic states, the most adapted experiments are those at low-temperature, and measurements resolved in space (e.g., microscopic) and/or in energy (e.g., narrowband).

B. Low-temperature experiments

Several temperature-dependent measurements have indicated a transition to localized states at low temperature. Luminescence experiments have given evidence of localization effects at low temperature, for instance, by observing the so-called S shape of the luminescence energy [49] or the localization edge in photoluminescence excitation measurements [50]. To date however, these measurements have not been interpreted in an excitonic framework but rather with free-particle models.

Recent photoemission (PE) quantum yield measurements in bulk *p*-doped InGaN materials displayed electron localization at low temperatures [51]. The mechanism invoked is the presence of the electron-hole interaction, as independent electrons states are delocalized [Fig. 2(a)]. The delocalization occurring at high temperatures may be due either to exciton ionization followed by electron transport or to thermally activated exciton motion: we note that both processes should have activation energies in the same range (20–30 meV, see Figs. 5 and 6). A detailed analysis of these results requires additional efforts, as the material contains equilibrium holes whose density depends on doping and temperature (only ionized acceptors yield unbound, localized holes). Nonetheless, these results open the door to further studies of exciton-mediated transport.

C. Measurements with high resolution (in space or energy)

Microscopic measurements should bring more detailed information on the energies and wave functions computed in this paper. However, they are still in their infancy and delicate to perform, as they require low temperature and localized carrier

injection/observation. For an order of magnitude, the QW plane can be partitioned into localization domains of ~ 3 nm; an optical experiment probing an area of 100 nm radius, with broadband wavelength resolution, would thus probe ~ 1000 low-energy states.

In Ref. [52], single narrow exciton emission lines were observed through small apertures which select few localization regions in InGaN/GaN QWs. This is a very promising technique; however, it has not been systematically used to assess the density of states. In fact, the very low areal density of lines observed appears incompatible with the density of localized states reported in this paper; this might indicate that defect-bound states are observed rather than those due to intrinsic compositional fluctuations (which should be much denser in the apertures used).

Another localized observation technique, scanning tunneling luminescence, is provided by the luminescence of localized carriers injected into QWs thanks to a scanning tunneling microscope tip [53]. Temperature-broadened peaks have been observed at room temperature in some samples (though here again, it remains unclear whether these are defect bound). The technique needs to be extended to low temperatures to yield narrow lines which will enable an assessment of energy distributions.

More advanced spectroscopic techniques could bring more detailed information to assess the results of this paper: resonant optical excitation provided by the joint use of small apertures and tunable source might interrogate a small number of states (either groundlike or excited states) in luminescent or resonant scattering experiments [54]. Figure 17 illustrates this. According to our results, the statistical spread of the ground state energy across configurations is on the order of 20 meV (or a wavelength spread of ~ 3 nm). Thus, a narrowband source with a few-gigahertz linewidth should be able to excite only one or a few states in a 100 nm aperture. Note, however, that this requires the intrinsic linewidth of each localized state to be narrow enough. This might be the case at low temperature, where homogeneous broadening is reduced. As another way to excite a small number of states, one might combine an aperture and low-energy excitation, deep enough in the Urbach tail. The Urbach energy is 25–30 meV, so that excitation 100 meV below the band edge (or more properly, below the energy at which the density of states reaches an approximate plateau) would lead to a reduction in the local density of states by 20–50 \times .

One may wonder about the intensity of the signal in such experiments, as the oscillator strength per localized exciton is strongly reduced compared with the areal oscillator strength in QWs (due to lateral extent and polarization fields). Nonetheless, experiments have shown that single-photon signals from single-quantum dots can be detected [55]. It is expected that excitons localized by disorder would have a similar oscillator strength.

Finally, the relative intensity of the longitudinal optical phonon replica could differentiate between the relative electron-hole motion thanks to the sensitivity of the Huang-Rhys factor to electron-hole separation and localization [56,57]. Exciton lifetime should also be a good indicator of electron-hole overlap of the exciton wave functions, widely varying, as seen in Figs. 8 and 9.

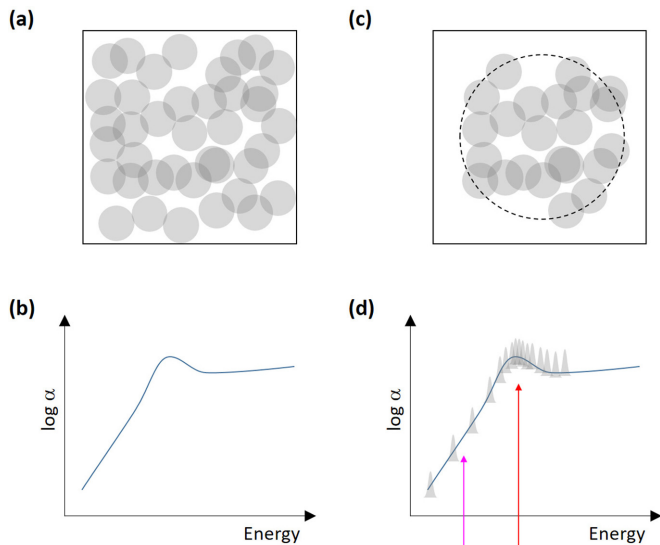


FIG. 17. Probing excitonic states with experiments. (a) Top view of a macroscopic sample, in which many localized (and delocalized) states, represented as gray circles, are probed. (b) Corresponding optical response: here, the optical absorption α , displaying an Urbach tail at low energy, an excitonic peak, and a slow variation at higher energy (where delocalized and free states contribute). (c) Top view of a sample with microscopic resolution, for instance, through a sub-micron aperture (circle): here, fewer states are probed. (d) The optical response should then reveal its underlying structure, composed of sharp excitonic resonances at low energy (gray peaks). Narrow-band resonant measurements in this region (red arrow) may be able to resolve a small number of localized excitonic states; alternatively, resonant measurements deep enough in the Urbach tail (pink arrow) where the density of states is sufficiently depleted might address a few states or even a single state.

D. InGaN excitons as quantum-optics emitters

In addition to simple optical transitions, another important topic is the possible use of these localized excitonic states to generate entangled photon pairs from biexciton recombinations, with applications in quantum optics. As emphasized in Ref. [18], in the case of InGaN quantum dots, this is predicated both on the magnitude of the exciton exchange energy and on the polarization selection rules of the emitted light.

Performing a similar study in our context would require a more complex framework than the simple two-band approximation considered in this paper. Below, we merely sketch a high-level roadmap to such a calculation.

At the lowest order, a three-band model, with one conduction band and two valence bands (e.g., considering S , P_x , and P_y orbitals) would be required to compute the polarization state of optical transitions (assuming a negligible contribution from P_z orbitals, a plausible approximation that would need to be validated separately). This would lead to a nine-dimensional Hamiltonian in real space once alloy disorder is included. Such a problem would be too complex numerically to be solved directly by our method. On the other hand, the quasiseparable approach of Sec. V could be used to separate this problem into two coupled problems, with 3D in the z direction and 6D in-plane. These problems could then be tackled with the same approach used in this paper, yielding three-band

excitonic wave functions, from which the polarization state of optical transitions would follow. The corresponding exchange interaction could then be computed as a perturbation, using overlap integrals like those of Ref. [58].

Reference [18] has shown that, in InGaN quantum dots, excitonic transitions do not generally fulfill the requirements for polarization-entangled emission, namely, a small-enough exchange energy, and two nearly degenerate exciton states with orthogonal polarizations; however, some random configurations might be suitable as quantum-optics emitters, though their likelihood of occurrence is unclear. With the approach we just outlined, one could seek to answer the same question for localized excitons in InGaN QWs: by repeating the computation for a sufficient number of configurations, one could then study the statistics of excitonic states that satisfy quantum-optics requirements.

VII. CONCLUSIONS

The properties of excitons in disordered InGaN QWs were studied numerically, revealing a strong dependence on the details of the QW design, thus justifying the need for the statistical exploration presented here. In general, trends are dominated by a competition between polarization fields, the Coulomb interaction, and the details of the InGaN configuration. Weakly bound excitons, for instance, those in thick QWs where electron-hole separation dominates the physics, can be thought of as uncorrelated electron-hole pairs with a Coulomb correction and a low binding energy; screening by free carriers further reduces these excitonic effects at intermediate carrier densities, precluding any significant impact such as exciton-mediated luminescence in conventional LEDs. On the other hand, in very thin and NP QWs, the excitonic interaction dominates the behavior, leading to binding energies as high as 100 meV and a complex wave function with a true 6D hybrid nature: the electron and hole are correlated, but their relative motion remains far from hydrogenoid. In such structures, macroscopic excitonic populations can be expected. Future experiments, ideally spectroscopy resolved in space and energy, might be necessary to probe the states studied here.

In perspective, in this paper, we pave the way to the study of a peculiar class of semiconductor quasiparticles: excitonic states in the presence of strong disorder. Under the right conditions, disorder enhances the Coulomb interaction and can lead to robust excitonic states at room temperature and high carrier density. InGaN compounds are an ideal testbed for these states, as the Coulomb interaction and disorder are of a similar magnitude, and their relative influence can further be controlled through material composition, design of the heterostructure, and even tunable parameters such as an applied electrical field. In addition to III-nitride, similar excitonic effects could also be investigated in other disordered materials with strong Coulomb interaction, such as some 2D semiconductors [59].

ACKNOWLEDGMENTS

C.W. was supported by the Simons Foundation (Grant No. 601954), the National Science Foundation RAISE program

(Grant No. DMS-1839077), and the French National Research Agency (ELENID Grant No. ANR-17-CE24-0040-01 and TECCLON Grant No. ANR-20-CE05-0037-01).

APPENDIX A: COMPUTATIONAL DETAILS

1. Schrödinger equation terms

The electrostatic potential is the sum of two terms: the *pin* junction potential V_J and the potential from the polarization fields V_P .

V_J is obtained assuming an abrupt junction, such that the junction field (considering the applied voltage, 3 V here) is dropped across the intrinsic region.

V_P is obtained conventionally by computing the strain equations and solving the resulting Poisson equation [60]. We first compute the electrical polarization P_z in the z direction (there, we assume that the piezoelectric constant e_{15} is zero since various works have found its effect to be small compared with other piezoelectric terms) [61]. We then derive the corresponding charge as $\rho = -\text{Div}(P_z)$ and finally the potential by inverting the Laplace equation $\Delta V_P = -\rho/\epsilon$ (with Δ the Laplacian operator and ϵ the dielectric constant). As boundary conditions in this equation, we assume a constant potential at both ends of the computation domain (a good approximation since the domain includes 3 nm of GaN on both sides of the QW, which is enough to smooth out the in-plane variations of V_P in the InGaN QW). Here, ϵ is taken equal to that of GaN, thus ignoring small local variations caused by alloy fluctuations. In other words, local field effects are ignored; note that their strength should be greatly reduced anyway since the QW does not have a sharp interface due to disorder.

Other details on the construction of the Hamiltonian can be found in the supplemental information of Ref. [28].

One open question when treating alloy disorder in the envelope approximation is the scale σ over which the atomic distribution of atoms should be averaged. In several previous works, a value of $\sigma = 0.3$ nm was used. Qualitatively, larger values of σ lead to a more smoothed-out potential (i.e., a reduce depth around In fluctuations) and therefore weaker localization.

We have explored numerically the effect of σ on E_B , considering values of 0.3 and 0.6 nm. As shown in Fig. 18, we find that the influence on E_B is moderate (typically $<10\%$ variation between these two values of σ). This is because, even though σ has some influence on the details of the electron and hole wave functions, the electron-hole overlap which governs excitonic interaction occurs on a scale larger than σ (several nanometers at least). Therefore, we conclude that our results are reasonably robust against the chosen value of σ .

The ITP method naturally has periodic boundary conditions, whereas the potential is not periodic. To circumvent this, we add a thin barrier with high potential energy (1 eV) at the edges of the computational domain to force wave functions to vanish there. The lateral dimensions of the computation domain are sufficient for this boxlike confinement to have a minute effect on the computed energies.

2. ITP method

The ITP method is based upon the SO method, which is an efficient approach to computing the time evolution of a wave

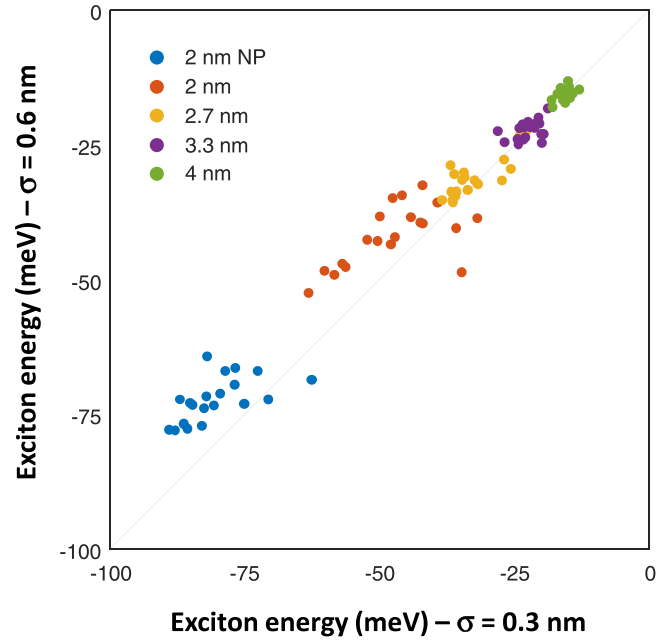


FIG. 18. Correlation between the binding energies obtained for values $\sigma = 0.3$ and 0.6 nm [each point is a configuration, with 10 configurations per QW design]. The effect on E_B is moderate. A smaller value of σ leads to slightly deeper confinement potentials and hence a slightly larger binding energy.

function. In the SO method, the Hamiltonian is split into its two components, the real-space potential term (including the Coulomb potential) and the reciprocal-space kinetic energy term: $H = H_r + H_k$.

The conventional SO method, which is accurate to second order in the time step dt , defines the following operators:

$$U_r = \exp\left(-\frac{iH_r dt}{2\hbar}\right), \quad (\text{A1})$$

$$U_k = \exp\left(-\frac{iH_k dt}{\hbar}\right). \quad (\text{A2})$$

The time propagation of the wave function from t to $t + dt$ is then obtained as follows:

$$\psi_1 = U_r \psi(t), \quad (\text{A3})$$

$$\psi_2 = \mathcal{F}(\psi_1), \quad (\text{A4})$$

$$\psi_3 = U_k \psi_2, \quad (\text{A5})$$

$$\psi_4 = \mathcal{F}^{-1}(\psi_3), \quad (\text{A6})$$

$$\psi(t + dt) = U_r \psi_4. \quad (\text{A7})$$

Here, \mathcal{F} and \mathcal{F}^{-1} are the direct and inverse Fourier transforms between real and momentum space. In other words, the wave function is propagated for a half-step in real space, a step in momentum space, and another half-step in real space, with Fourier transforms in between to transition between real and momentum space. The SO scheme is computationally efficient because it only relies on matrix multiplications and Fourier transforms.

In this paper, we use a further improvement of the SO scheme, with fourth-order accuracy [36,37]. We define the operators:

$$U_{r1} = \exp\left(-\frac{iH_r dt}{6\hbar}\right), \quad (\text{A8})$$

$$U_{r2} = \exp\left(-\frac{iH_r 2dt}{3\hbar}\right), \quad (\text{A9})$$

$$U_k = \exp\left(-\frac{iH_k dt}{2\hbar}\right). \quad (\text{A10})$$

The time propagation is given by

$$\psi_1 = U_{r1} \psi(t), \quad (\text{A11})$$

$$\psi_2 = \mathcal{F}(\psi_1), \quad (\text{A12})$$

$$\psi_3 = U_k \psi_2, \quad (\text{A13})$$

$$\psi_4 = \mathcal{F}^{-1}(\psi_3), \quad (\text{A14})$$

$$\psi_5 = U_{r2} \psi_4, \quad (\text{A15})$$

$$\psi_6 = \mathcal{F}(\psi_5), \quad (\text{A16})$$

$$\psi_7 = U_k \psi_6, \quad (\text{A17})$$

$$\psi_8 = \mathcal{F}^{-1}(\psi_7), \quad (\text{A18})$$

$$\psi(t+dt) = U_{r1} \psi_8. \quad (\text{A19})$$

If dt is real, the SO method yields standard time propagation. If dt is complex, we obtain the ITP method: starting from a trial wave function of arbitrary shape, the wave function decays toward the ground state as it is propagated.

We find that an appropriate time step is given by $\hbar dt = 10/\Delta H_r$, where ΔH_r is the difference between the minimum and maximum values of H_r across the simulation domain. A few tens of steps are sufficient to reach energy convergence on the order of 1 meV.

APPENDIX B: ABC SCHEME

The ABC scheme was introduced in Ref. [34]. It properly regularizes divergent operators on finite difference grids. In our case, the discretized radius operator is defined accordingly by

$$\begin{aligned} \frac{1}{\bar{r}} = & \frac{1}{2} \left[\sqrt{\frac{(i+1)^2}{dx^2} + \frac{j^2}{dy^2} + \frac{k^2}{dz^2}} + \sqrt{\frac{(i-1)^2}{dx^2} + \frac{j^2}{dy^2} + \frac{k^2}{dz^2}} + \sqrt{\frac{i^2}{dx^2} + \frac{(j+1)^2}{dy^2} + \frac{k^2}{dz^2}} \right. \\ & \left. + \sqrt{\frac{i^2}{dx^2} + \frac{(j-1)^2}{dy^2} + \frac{k^2}{dz^2}} + \sqrt{\frac{i^2}{dx^2} + \frac{j^2}{dy^2} + \frac{(k+1)^2}{dz^2}} + \sqrt{\frac{i^2}{dx^2} + \frac{j^2}{dy^2} + \frac{(k-1)^2}{dz^2}} \right] \\ & - 3 \sqrt{\frac{i^2}{dx^2} + \frac{j^2}{dy^2} + \frac{k^2}{dz^2}}, \end{aligned} \quad (\text{B1})$$

where (dx, dy, dz) are the mesh steps, i is defined as

$$i = \frac{X_e - X_h}{dx}, \quad (\text{B2})$$

and similar equations define j and k . Notice the nontrivial $+1$ and -1 terms, which distinguish the ABC scheme from the conventional discretization of $1/r$.

APPENDIX C: HYDROGENOID FACTORIZATION

We first project Ψ along z_e and z_h to obtain a 4D in-plane wave function:

$$\chi_{xy} = \left(\iint \Psi^2 dz_e dz_h \right)^{1/2}. \quad (\text{C1})$$

As elsewhere in this paper, the use of square roots is safe since we are dealing with ground-state wave functions which are real valued and positive.

The task is then to approximately factorize χ_{xy} in the form $\psi_{\text{abs}}(\mathbf{R}) \otimes \psi_{\text{rel}}(\mathbf{r})$.

We begin with the computation of the relative-movement wave function $\psi_{\text{rel}}(\mathbf{r})$. As a reminder, \mathbf{r} is the relative in-plane

movement, i.e., a 2D vector with coordinates $(x_h - x_e)$ and $(y_h - y_e)$.

Since the computation domain is discretized, \mathbf{r} can take a discrete number of values \mathbf{r}_i . For each of these, we find the set of indices $\{j\}$ of the spatial grid corresponding to \mathbf{r}_i . We then define the average value of χ_{xy} at position \mathbf{r}_i as

$$\chi_i = (\langle \chi^2 \rangle_{\{j\}})^{1/2}, \quad (\text{C2})$$

where $\langle \cdot \rangle_{\{j\}}$ denotes averaging over the set j . We then assign this average value to all points for which $\mathbf{r} = \mathbf{r}_i$, i.e., we set $\psi_{\text{rel}} = \chi_i$ for all points in the set $\{j\}$.

A similar procedure is followed to define $\psi_{\text{abs}}(\mathbf{R})$. The tensorial product $\psi_{\text{abs}}(\mathbf{R}) \otimes \psi_{\text{rel}}(\mathbf{r})$ yields the final factorization.

To validate this procedure, we first checked it by applying it to various numerically generated hydrogenoid wave functions (these were defined in real-space coordinates rather than in hydrogenoid coordinates, with the expectation that the hydrogenoid factorization should be highly accurate). In these tests, we found values of $O_{\text{hydro}} > 0.99$, confirming the validity of our approach.

In practice, however, for the wave functions computed in this paper, O_{hydro} never reaches such high values due to the

restricted size of the computation domain. For instance, an exciton in GaN (i.e., without any alloy fluctuations) yields $O_{\text{hydro}} \sim 0.92$, even though the corresponding wave function should be hydrogenoid if the computation domain was infinite. When InGaN alloy fluctuations are introduced and the

wave function loses its hydrogenoid nature, O_{hydro} drops to lower values ~ 0.5 – 0.8 .

In summary, O_{hydro} is indicative of the hydrogenoid nature of a wave function, keeping in mind that values >0.9 indicate a strongly hydrogenoid nature.

-
- [1] R. S. Knox, *Theory of Excitons*, Solid State Physics, Vol. 5 (Academic Press, New York, 1963).
- [2] D. S. Chemla, D. Miller, P. Smith, A. Gossard, and W. Wiegmann, Room temperature excitonic nonlinear absorption and refraction in GaAs/AlGaAs multiple quantum well structures, *IEEE J. Quantum Electron.* **20**, 265 (1984).
- [3] S. D. Baranovskii and A. L. Efros, Band edge smearing in solid solutions, *Sov. Phys. Semicond.* **12**, 1328 (1978).
- [4] E. F. Schubert, E. O. Göbel, Y. Horikoshi, K. Ploog, and H. J. Queisser, Alloy broadening in photoluminescence spectra of $\text{Al}_x\text{Ga}_{1-x}\text{As}$, *Phys. Rev. B* **30**, 813 (1984).
- [5] S. Permogorov and A. Reznitsky, Effect of disorder on the optical spectra of wide-gap II–VI semiconductor solid solutions, *J. Lumin.* **52**, 201 (1992).
- [6] H. Masenda, L. M. Schneider, M. Adel Aly, S. J. Machchhar, A. Usman, K. Meerholz, F. Gebhard, S. D. Baranovskii, and M. Koch, Energy scaling of compositional disorder in ternary transition-metal dichalcogenide monolayers, *Adv. Electron. Mater.* **7**, 2100196 (2021).
- [7] H. Fidder, J. Terpstra, and D. A. Wiersma, Dynamics of Frenkel excitons in disordered molecular aggregates, *J. Chem. Phys.* **94**, 6895 (1991).
- [8] F. Würthner, T. E. Kaiser, and C. R. Saha-Moller, J-aggregates: from serendipitous discovery to supramolecular engineering of functional dye materials, *Angew. Chem., Int. Ed.* **50**, 3376 (2011).
- [9] D. V. Makhov and W. Barford, Local exciton ground states in disordered polymers, *Phys. Rev. B* **81**, 165201 (2010).
- [10] A. V. Rodina, M. Dietrich, A. Goldner, L. Eckey, A. Hoffmann, A. L. Efros, M. Rosen, and B. K. Meyer, Free excitons in wurtzite GaN, *Phys. Rev. B* **64**, 115204 (2001).
- [11] S. Chichibu, T. Sota, K. Wada, and S. Nakamura, Exciton localization in InGaN quantum well devices, *J. Vac. Sci. Technol. B* **16**, 2204 (1998).
- [12] Y. Kawakami, Y. Narukawa, K. Omae, S. Fujita, and S. Nakamura, Dimensionality of excitons in InGaN-based light emitting devices, *Phys. Status Solidi A* **178**, 331 (2000).
- [13] T. Bartel, M. Dworzak, M. Strassburg, A. Hoffmann, A. Strittmatter, and D. Bimberg, Recombination dynamics of localized excitons in InGaN quantum dots, *Appl. Phys. Lett.* **85**, 1946 (2004).
- [14] G. Rossbach, J. Levrat, G. Jacopin, M. Shahmohammadi, J. F. Carlin, J. D. Ganiere, R. Butte, B. Deveaud, and N. Grandjean, High-temperature Mott transition in wide-band-gap semiconductor quantum wells, *Phys. Rev. B* **90**, 201308(R) (2014).
- [15] A. Hangleiter, Z. Jin, M. Gerhard, D. Kalincev, T. Langer, H. Bremers, U. Rossow, M. Koch, M. Bonn, and D. Turchinovich, Efficient formation of excitons in a dense electron-hole plasma at room temperature, *Phys. Rev. B* **92**, 241305(R) (2015).
- [16] W. Liu, R. Butte, A. Dussaigne, N. Grandjean, B. Deveaud, and G. Jacopin, Carrier-density-dependent recombination dynamics of excitons and electron-hole plasma in *m*-plane InGaN/GaN quantum wells, *Phys. Rev. B* **94**, 195411 (2016).
- [17] D. Bayerl and E. Kioupakis, Room-temperature stability of excitons and transverse-electric polarized deep-ultraviolet luminescence in atomically thin GaN quantum wells, *Appl. Phys. Lett.* **115**, 131101 (2019).
- [18] S. K. Patra and S. Schulz, Indium gallium nitride quantum dots: consequence of random alloy fluctuations for polarization entangled photon emission, *Mater. Quantum Technol.* **1**, 015001 (2021).
- [19] D. Watson-Parris, M. J. Godfrey, P. Dawson, R. A. Oliver, M. J. Galtrey, M. J. Kappers, and C. J. Humphreys, Carrier localization mechanisms in $\text{In}_x\text{Ga}_{1-x}\text{N}$ /GaN quantum wells, *Phys. Rev. B* **83**, 115321 (2011).
- [20] S. Schulz, M. A. Caro, C. Coughlan, and E. P. O'Reilly, Atomistic analysis of the impact of alloy and well-width fluctuations on the electronic and optical properties of InGaN/GaN quantum wells, *Phys. Rev. B* **91**, 035439 (2015).
- [21] M. Auf der Maur, A. Pecchia, G. Penazzi, W. Rodrigues, and A. Di Carlo, Efficiency Drop in Green InGaN/GaN Light Emitting Diodes: The Role of Random Alloy Fluctuations, *Phys. Rev. Lett.* **116**, 027401 (2016).
- [22] M. Piccardo, C.-K. Li, Y.-R. Wu, J. S. Speck, B. Bonef, R. M. Farrell, M. Filoche, L. Martinelli, J. Peretti, and C. Weisbuch, Localization landscape theory of disorder in semiconductors. II. Urbach tails of disordered quantum well layers, *Phys. Rev. B* **95**, 144205 (2017).
- [23] C.-K. Li, M. Piccardo, L.-S. Lu, S. Mayboroda, L. Martinelli, J. Peretti, J. S. Speck, C. Weisbuch, M. Filoche, and Y.-R. Wu, Localization landscape theory of disorder in semiconductors. III. Application to carrier transport and recombination in light emitting diodes, *Phys. Rev. B* **95**, 144206 (2017).
- [24] C. M. Jones, C.-H. Teng, Q. Yan, P.-C. Ku, and E. Kioupakis, Impact of Carrier Localization on Recombination in InGaN Quantum Wells and the Efficiency of Nitride Light-Emitting Diodes: Insights from Theory and Numerical Simulations, *Appl. Phys. Lett.* **111**, 113501 (2017).
- [25] D. S. P. Tanner, J. M. McMahon, and S. Schulz, Interface Roughness, Carrier Localization, and Wave Function Overlap in *c*-Plane (In, Ga)N/GaN Quantum Wells: Interplay of Well Width, Alloy Microstructure, Structural Inhomogeneities, and Coulomb Effects, *Phys. Rev. Appl.* **10**, 034027 (2018).
- [26] S. K. Patra and S. Schulz, Exploring the potential of *c*-plane indium gallium nitride quantum dots for twin-photon emission, *Nano Lett.* **20**, 234 (2020).
- [27] D. S. P. Tanner and S. Schulz, Electronic and excitonic properties of ultrathin (In, Ga) N layers: the role of

- alloy and monolayer width fluctuations, *Nanoscale* **12**, 20258 (2020).
- [28] A. David, N. G. Young, and M. D. Craven, Many-Body Effects in Strongly Disordered III-Nitride Quantum Wells: Interplay Between Carrier Localization and Coulomb Interaction, *Phys. Rev. Appl.* **12**, 044059 (2019).
- [29] P. Bigenwald, P. Lefebvre, T. Bretagnon, and B. Gil, Confined excitons in GaN-AlGaIn quantum wells, *Phys. Status Solidi B* **216**, 371 (1999).
- [30] H. G. Park, S. H. Kim, S. H. Kwon, Y. G. Ju, J. K. Yang, J. H. Baek, S. B. Kim, and Y. H. Lee, Electrically driven single-cell photonic crystal laser, *Science* **305**, 1444 (2004).
- [31] A semantic note on the use of the term *exciton* in the context of disordered materials: as remarked by Combescot *et al.* [62], localized electron-hole pairs differ fundamentally from delocalized excitons, for instance, lacking momentum conservation in light absorption. For simplicity, we will nonetheless use the term exciton throughout and will discuss how the present wave functions differ from delocalized excitons.
- [32] S. Glutsch, D. S. Chemla, and F. Bechstedt, Numerical calculation of the optical absorption in semiconductor quantum structures, *Phys. Rev. B* **54**, 11592 (1996).
- [33] S. Glutsch, *Excitons in Low-Dimensional Semiconductors: Theory Numerical Methods Applications*, Vol. 141 (Springer, Berlin, Heidelberg, 2004).
- [34] A. Gordon, C. Jiruschek, and F. X. Kartner, Numerical solver of the time-dependent Schrödinger equation with Coulomb singularities, *Phys. Rev. A* **73**, 042505 (2006).
- [35] L. Lehtovaara, J. Toivanen, and J. Eloranta, Solution of time-independent Schrödinger equation by the imaginary time propagation method, *J. Comput. Phys.* **221**, 148 (2007).
- [36] A. Bandrauk and H. Shen, Exponential split operator methods for solving coupled time-dependent Schrödinger equations, *J. Chem. Phys.* **99**, 1185 (1993).
- [37] J. Auer, E. Krotscheck, and S. A. Chin, A fourth-order real-space algorithm for solving local Schrödinger equations, *J. Chem. Phys.* **115**, 6841 (2001).
- [38] A. V. Kavokin, Exciton oscillator strength in quantum wells: from localized to free resonant states, *Phys. Rev. B* **50**, 8000 (1994).
- [39] Note that this equality relates the square modulus of wave functions. For the ground state, which is real-valued and positive, we can safely define $\psi = \sqrt{\psi^2}$.
- [40] A. David and M. J. Grundmann, Influence of polarization fields on carrier lifetime and recombination rates in InGaIn-based light-emitting diodes, *Appl. Phys. Lett.* **97**, 033501 (2010).
- [41] Y. Zhang and A. Mascarenhas, Scaling of exciton binding energy and virial theorem in semiconductor quantum wells and wires, *Phys. Rev. B* **59**, 2040 (1999).
- [42] H. Haug and S. W. Koch, *Quantum Theory of the Optical and Electronic Properties of Semiconductors*, 5th ed. (World Scientific Publishing Company, Singapore, 2009).
- [43] A. David and M. J. Grundmann, Droop in InGaIn light-emitting diodes: a differential carrier lifetime analysis, *Appl. Phys. Lett.* **96**, 103504 (2010).
- [44] D. Snoke, Predicting the ionization threshold for carriers in excited semiconductors, *Solid State Commun.* **146**, 73 (2008).
- [45] D. Cherns and C. G. Jiao, Electron Holography Studies of the Charge on Dislocations in GaN, *Phys. Rev. Lett.* **87**, 205504 (2001).
- [46] R. A. Oliver, S. E. Bennett, T. Zhu, D. J. Beesley, M. J. Kappers, D. W. Saxey, A. Cerezo, and C. J. Humphreys, Microstructural origins of localization in InGaIn quantum wells, *J. Phys. D* **43**, 354003 (2010).
- [47] R. Butte, L. Lahourcade, T. K. Uzdavinys, G. Callsen, M. Mensi, M. Glauser, G. Rossbach, D. Martin, J.-F. Carlin, and S. Marcinkevicius, Optical absorption edge broadening in thick InGaIn layers: random alloy atomic disorder and growth mode induced fluctuations, *Appl. Phys. Lett.* **112**, 032106 (2018).
- [48] G. Callsen, R. Butte, and N. Grandjean, Probing Alloy Formation Using Different Excitonic Species: The Particular Case of InGaIn, *Phys. Rev. X* **9**, 031030 (2019).
- [49] Y.-H. Cho, G. H. Gainer, A. J. Fischer, J. J. Song, S. Keller, U. K. Mishra, and S. P. DenBaars, S-shaped temperature-dependent emission shift and carrier dynamics in InGaIn/GaN multiple quantum wells, *Appl. Phys. Lett.* **73**, 1370 (1998).
- [50] S. Schulz, D. S. P. Tanner, E. P. O'Reilly, M. A. Caro, F. Tang, J. T. Griffiths, F. Oehler, M. J. Kappers, R. A. Oliver, and C. J. Humphreys, Theoretical and experimental analysis of the photoluminescence and photoluminescence excitation spectroscopy spectra of *m*-plane InGaIn/GaN quantum wells, *Appl. Phys. Lett.* **109**, 223102 (2016).
- [51] M. Sauty, N. Lopes, J.-P. Banon, Y. Lassailly, L. Martinelli, A. Alhassan, S. Nakamura, J. S. Speck, C. Weisbuch, and J. Peretti, Evidence of localization effect on photoelectron transport induced by alloy disorder in nitride semiconductor compounds, [arXiv:2201.03278](https://arxiv.org/abs/2201.03278).
- [52] H. Schömig, S. Halm, A. Forchel, G. Bacher, J. Off, and F. Scholz, Probing Individual Localization Centers in an InGaIn/GaN Quantum Well, *Phys. Rev. Lett.* **92**, 106802 (2004).
- [53] W. Hahn, J. M. Lentali, P. Polovodov, N. Young, S. Nakamura, J. S. Speck, C. Weisbuch, M. Filoche, Y. R. Wu, M. Piccardo, *et al.*, Evidence of nanoscale Anderson localization induced by intrinsic compositional disorder in InGaIn/GaN quantum wells by scanning tunneling luminescence spectroscopy, *Phys. Rev. B* **98**, 045305 (2018).
- [54] V. Bellani, M. Amado, E. Diez, C. Koerdts, M. Potemski, and R. Hey, Resonant Rayleigh scattering in ordered and disordered semiconductor superlattices, *Phys. Rev. B* **76**, 075349 (2007).
- [55] M. Arita, T. Iki, M. J. Holmes, and Y. Arakawa, Single photon generation from AlGaIn exciton localization centers exhibiting narrow spectral linewidths, *APL Mater.* **9**, 121106 (2021).
- [56] D. M. Graham, A. Soltani-Vala, P. Dawson, M. J. Godfrey, T. M. Smeeton, J. S. Barnard, M. J. Kappers, C. J. Humphreys, and E. J. Thrush, Optical and microstructural studies of InGaIn-GaN single-quantum-well structures, *J. Appl. Phys.* **97**, 103508 (2005).
- [57] Y. Zhang, Applications of Huang-Rhys theory in semiconductor optical spectroscopy, *J. Semicond.* **40**, 091102 (2019).
- [58] E. Kadantsev and P. Hawrylak, Theory of exciton fine structure in semiconductor quantum dots: quantum dot anisotropy and lateral electric field, *Phys. Rev. B* **81**, 045311 (2010).
- [59] A. F. Rigosi, H. M. Hill, K. T. Rim, G. W. Flynn, and T. F. Heinz, Electronic band gaps and exciton binding energies in monolayer Mo_xW_{1-x}S₂ transition metal dichalcogenide alloys probed by scanning tunneling and optical spectroscopy, *Phys. Rev. B* **94**, 075440 (2016).
- [60] U. M. E. Christmas, A. D. Andreev, and D. A. Faux, Calculation of electric field and optical transitions in InGaIn/GaN quantum wells, *J. Appl. Phys.* **98**, 073522 (2005).

- [61] S. Schulz, A. Berube, and E. P. O'Reilly, Polarization fields in nitride-based quantum dots grown on nonpolar substrates, [Phys. Rev. B](#) **79**, 081401(R) (2009).
- [62] M. Combescot, V. Voliotis, and S.-Y. Shiau, Fundamental differences between exciton and quantum dot duo, [Semicond. Sci. Technol.](#) **35**, 045013 (2020).